



HAL
open science

On the determination of coherent solar climates over a tropical island with a complex topography.

Pauline Mialhe, Benjamin Pohl, Béatrice Morel, Jörg Trentmann, Guillaume Jumaux, François Bonnardot, Miloud Bessafi, Jean-Pierre Chabriat

► **To cite this version:**

Pauline Mialhe, Benjamin Pohl, Béatrice Morel, Jörg Trentmann, Guillaume Jumaux, et al.. On the determination of coherent solar climates over a tropical island with a complex topography.. Solar Energy, 2020, 206, pp.508-521. 10.1016/j.solener.2020.04.049 . hal-02901907

HAL Id: hal-02901907

<https://hal.science/hal-02901907v1>

Submitted on 21 Jun 2022

HAL is a multi-disciplinary open access archive for the deposit and dissemination of scientific research documents, whether they are published or not. The documents may come from teaching and research institutions in France or abroad, or from public or private research centers.

L'archive ouverte pluridisciplinaire **HAL**, est destinée au dépôt et à la diffusion de documents scientifiques de niveau recherche, publiés ou non, émanant des établissements d'enseignement et de recherche français ou étrangers, des laboratoires publics ou privés.



Distributed under a Creative Commons Attribution - NonCommercial 4.0 International License

On the determination of coherent solar climates over a tropical island with a complex topography

Mialhe Pauline^{a,b}, Pohl Benjamin^b, Morel Béatrice^a, Jörg Trentmann^c, Jumaux Guillaume^d, Bonnardot François^d, Bessafi Miloud^a, Chabriat Jean-Pierre^a

^aLaboratoire d'Énergie, d'Électronique et Procédés (LE2P), Université de La Réunion, La Réunion, France

^bCentre de Recherche de Climatologie (CRC), UMR 6282 Biogéosciences, CNRS/Université de Bourgogne Franche-Comté, Dijon, France

^cDeutscher Wetterdienst, Satellite-based Climate Monitoring, Frankfurter Str. 135, 63067 Offenbach, Germany

^dMétéo-France, Direction Interrégionale pour l'Océan Indien, La Réunion, France

Abstract

Many tropical islands are aiming at a greener self-sufficient energy production based on renewable energy, notably solar-generated electricity. This work explores the mean solar cycles over La Réunion (southwest Indian Ocean: 21°S, 55.5°E) and their spatial behavior using the Solar surface RADIation Heliosat - East (SARAH-E) satellite data at high spatial and time resolutions (0.05°, hourly data over 1999-2016). Comparisons of SARAH-E satellite-derived data with ground-based measurements show differences of 15 % for diurnal-seasonal variations. The solar resource over the island has strong spatial variability, with differences larger than 100 W.m⁻² between coastal and mountainous zones. The mean solar resource is more than 20 % lower on the island than on the nearby sea. The strongest interaction between diurnal and annual cycles are found at the windward mid-slopes and at the active volcano, related to well-known cloud processes. A clustering of solar zones, based on diurnal-seasonal means, structures the island into a West/East dipole balancing the solar energy in a day through the year.

Keywords: Surface solar radiation, La Réunion island, Complex meteorological context, Seasonal/diurnal cycles, Cluster analysis, SARAH-E

1. Introduction

Climate changes are leading to a major adaptation of the energy system and strategies (IPCC-WGII, 2014). This emulation has led the smart- and micro-grid concepts to appear. They are the next upgrade of our current power grid model (Hirsch et al., 2018; Clastres, 2011). They aim at increasing the efficiency of the power grid while ensuring greener energy production for countries, cities and even smaller districts (Unamuno and Barrena, 2015).

This challenge is more a need for isolated areas, notably for those dependent on fossil fuels (e.g. Timilsina and Shah, 2016). This is especially the case for small islands (e.g. Mendoza-Vizcaino et al., 2019; Praene et al., 2012),

Email address: pauline.mialhe@univ-reunion.fr (Mialhe Pauline)

8 which face severe energy security issues (Kuang et al., 2016; Raghoo et al., 2018). Though highly variable, renew-
9 able energy resources there can be abundant, which gives opportunities to explore for renewable power conversion
10 (Weisser, 2004; Praene et al., 2012; Blechinger et al., 2016). Some of these islands have started to build models for
11 greener self-sufficient energy production (e.g. Bağcı, 2009; Praene et al., 2012; Gils and Simon, 2017; Meschede et al.,
12 2018; Obara et al., 2018; Mendoza-Vizcaino et al., 2019) that can be carried over to other islands (Meschede et al.,
13 2016, 2018; Surroop et al., 2018). Quarters, cities and even bigger power grids also benefit from the technical and
14 economic improvement resulting from the development of renewable energy use (e.g. Sen et al., 2016; Singh, 2018).
15 Islands are then becoming study cases for the development of renewable energy and probably map the road for the
16 future energy supply in the world (e.g. Notton, 2015; Bénard-Sora and Praene, 2018; Krajačić et al., 2011). Research
17 on the development of renewable energy in isolated areas is now being addressed as part of new models of global
18 energy self-sufficiency.

19 The solar resource has by far the highest energy potential on Earth (Perez et al., 2016). However, its intermittent
20 character is the greatest obstacle to the seamless integration of solar generated power into the power grids (Scorah
21 et al., 2012; Lauret et al., 2016; Blaga et al., 2019). The total amount of solar energy reaching the ground is modulated
22 at different timescales (Perez et al., 2016) by many factors, mostly cloud cover and the position of the sun (Marquez
23 and Coimbra, 2012). Forecasts try to anticipate short-term energy losses and to estimate future trend in the resource
24 potential (Antonanzas et al., 2016). Hybrid energy systems combine forecasts with storage and production alterna-
25 tives when the load differs from the incoming energy. This involves a correctly-sized storage system with energy
26 production alternatives (Colmenar-Santos et al., 2019; Akbari et al., 2018). Seasonal and diurnal cycles may give
27 useful information, which needs to be completed by site specifications (for instance due to topographic or climatic
28 particularities: Práválie et al., 2019; Singh Doorga et al., 2019; Al Garni and Awasthi, 2017; Perdigão et al., 2017;
29 Diabaté et al., 2004). The detailed knowledge of the solar resource and its spatial distribution are crucial for its pen-
30 etration in the energy mix of any power grid (e.g. Polo et al., 2015; Wegertseder et al., 2016; Fouilloy et al., 2018;
31 Singh Doorga et al., 2019; Koo et al., 2019). Optimized geographic allotment of PV plants smooths the impact of the
32 solar variability (Urquhart et al., 2013; Lave et al., 2012; Olowu et al., 2018) and acts to reduce the cost of the solar
33 energy (Perez and Fthenakis, 2015; Perez et al., 2019). Forecasts are usually improved when considering coherent
34 spatial zones (Koo et al., 2019) and their typical scales of variability (Fouilloy et al., 2018; Mejia et al., 2018).

35 La Réunion (21°S, 55.5°E), our case study, is a French tropical island and one of the outermost regions of the
36 European Union, in the South West Indian Ocean (SWIO). Since the mid-1980s, the island has experienced one of the
37 fastest transition of its demography (Bénard-Sora and Praene, 2016). The number of inhabitants was just more than
38 860,000 in 2017 and should exceed 1 million by 2037 (Merceron, 2017). The resulting increase in energy demand has
39 induced and will continue to induce major changes to the power grid of the island. Hydropower was producing 99 % of
40 electric demand in 1982 and only 30 % in 2002, when the politics started to turn the strong dependence of the island on
41 imported oil into a greener energy self-sufficiency (RégionRéunion, 2003a,b). In 2017, 32.4 % of La Réunion electric
42 mix was from renewable energy sources with 14 % from hydropower (OER, 2018). The large variability of the local

43 climate of La Réunion still limits the integration of renewable energy in the electric mix (Bénard-Sora and Praene,
44 2018; Diagne et al., 2013). The island wants to build a self-sufficiency only based on its renewable resources and
45 become a “zero-net energy” island (Praene et al., 2012; Selosse et al., 2018a). The local research aims at completing
46 and deepening the knowledge required to better exploit renewable energies, notably Surface Solar Radiation (SSR).

47 The solar resource strongly varies in both space and time over La Réunion island (Bessafi et al., 2018b; Badosa
48 et al., 2015, 2013; Jumaux et al., 2011). Both of these scales of variation need to be described to improve the solar
49 energy use. Few studies exist focusing on either the diurnal or the annual cycle of SSR. In addition, some of them are
50 based on ground-based measurements essentially at low and mid altitudes performed by the national weather service
51 (Météo-France), though more than 80 % of the island lies above 200 meters. Badosa et al. (2013) classified the diurnal
52 cycle into 5 daily regimes of SSR using data over 2 years (2007-2008) from 7 coastal and low altitude Météo-
53 France stations (9-186 meters). Météo-France published two climate atlases using data from their measuring network
54 (Soler, 1997; Jumaux et al., 2011). Jumaux et al. (2011) reconstructed monthly SSR maps using data over 10 years
55 (2001-2010) from 32 stations mainly at low and mid altitudes. Recently, monthly SSR maps were derived from the
56 Solar surfAce RAdiation Heliosat - East (SARAH-E; Huld et al., 2016) satellite dataset to describe the SSR patterns
57 at higher elevations over the island (Bessafi et al., 2018b). The present paper complements the aforementioned studies
58 by describing the spatial features of the diurnal cycle. It also specifies the intersection of the two orbital components
59 (namely, the diurnal and annual cycles), which have spatial particularities and can separate the island into coherent
60 zones of SSR. To that end, we use the Solar surfAce RAdiation Heliosat - East (SARAH-E) dataset which provides
61 SSR data over a long time period (from 1999 to 2016) at a high spatial resolution ($0.05^\circ \times 0.05^\circ$). The purpose of the
62 present study is to:

- 63 1. describe the SSR diurnal cycle which was previously defined only at coastal and mid-elevated weather stations,
- 64 2. underline the intersection of the two orbital components of solar irradiance and its related spatial spread over
65 the island,
- 66 3. identify, for the first time, favorable / complementary SSR zones for solar energy applications.

67 Section 2 describes La Réunion island case study, SARAH-E satellite dataset and the methods used. Section 3
68 presents the local solar context of the island with its related spatial SSR structures and section 4 the solar potential
69 zones as obtained from clustering. Finally, a discussion and some concluding remarks are developed in section 5.

70 2. Context, data and methods

71 2.1. The study case of La Réunion island

72 Figure 1(a) describes the topography of the island and locates its two highest peaks. The first one is the dormant
73 Piton des Neiges volcano at 3,071 m above sea level (asl) and the other one is the active Piton de La Fournaise volcano
74 at 2,560 m asl. They are separated by a 1,500 m-high plateau making the island an isolated and especially prominent
75 obstacle to the atmospheric circulations in the SWIO (Figure 2).

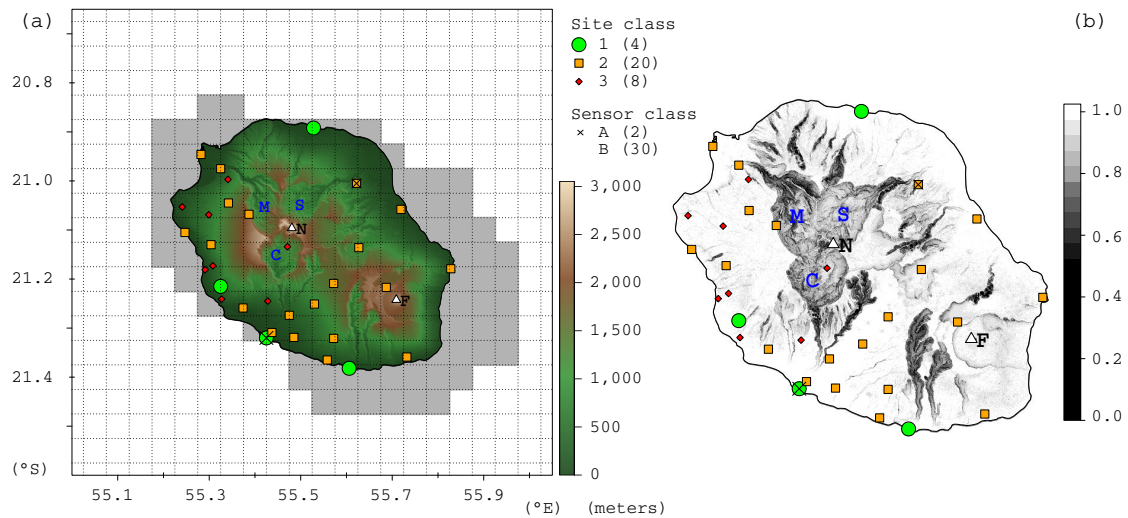


Figure 1: Topographical characteristics of La Réunion island : (a) elevation (in m) map based on SARAH-E grids (dotted gray lines). The pixels in grey locate where the island changes sea SSR. (b) the sky view factor map (unitless). Both maps are based on the Digital Elevation Model from [NASA Jet Propulsion Laboratory \(2009\)](#). The letters in blue stand for Cilaos (C), Mafate (M) and Salazie (S) Cirques; the triangles locate the volcanos : Le Piton de La Fournaise (F) and Le Piton des Neiges (N). Symbols refer to the WMO classification for site (1 to 3) and sensors (A to B). Sites classed 1 have no shade at ± 3 degrees above the local horizon, class 2 at ± 5 degrees and class 3 at ± 7 degrees. Sensors classified A are more precise than the B.

76 The island is mainly under an east-southeast trade wind (*e.g.* [Badosa et al., 2015](#); [Baldy et al., 1996](#)), which
 77 changes in direction according to the season: easterly in summer and more southeasterly in winter ([Figure 2](#); [Lesouëf](#)
 78 [et al., 2011](#)). This main flow is more a “flow around” than a “flow over” regime. The latter particularly occurs during
 79 violent wind conditions, such as tropical cyclones (TC). The main cloud regimes over La Reunion are (a) orographic
 80 clouds generated by the local topography and (b) clouds caught on the island driven by synoptic systems ([André et al.,](#)
 81 [2019](#); [Cécé et al., 2016](#); [Badosa et al., 2015](#); [Garrett, 1980](#)). The vertical development of the clouds in these two
 82 regimes is limited by the thermal inversion whose height over La Réunion ranges from 1,700 to 3,100 meters, with
 83 an average value of $\sim 2,000$ m ([Bhugwant et al., 2000](#); [Guilpart et al., 2017](#); [Réchou et al., 2019](#)). Recently, [Vérèmes](#)
 84 [et al. \(2019\)](#) found two peaks of cloud occurrence in the SWIO, the first one related to deep convection in summer
 85 and the other one to predominant liquid clouds at low altitudes in winter.

86 Associated precipitations vary according to elevation, with maximum amounts at 650 m asl along the windward
 87 slopes ([Réchou et al., 2019](#); [Sisavath et al., 2011](#)). In addition, the island experiences extreme events such as heavy
 88 rainfalls and storms as well as TC whose effects on rainfall are enhanced by the marked topography ([Jumaux et al.,](#)
 89 [2011](#); [Morel et al., 2014](#); [Pohl et al., 2016](#); [Leroux et al., 2018](#)). During TC Gamede, extreme rainfalls reached two
 90 world records of 3, 930 mm over 72 hours and 4, 936 mm over 4 days ([Quetelard et al., 2009](#)).

91 Factors modulating SSR variability include clouds and their intrinsic characteristics (for instance: extension,
 92 shape, depth) but also aerosols and water vapor in the air column, especially under clear sky conditions, and site

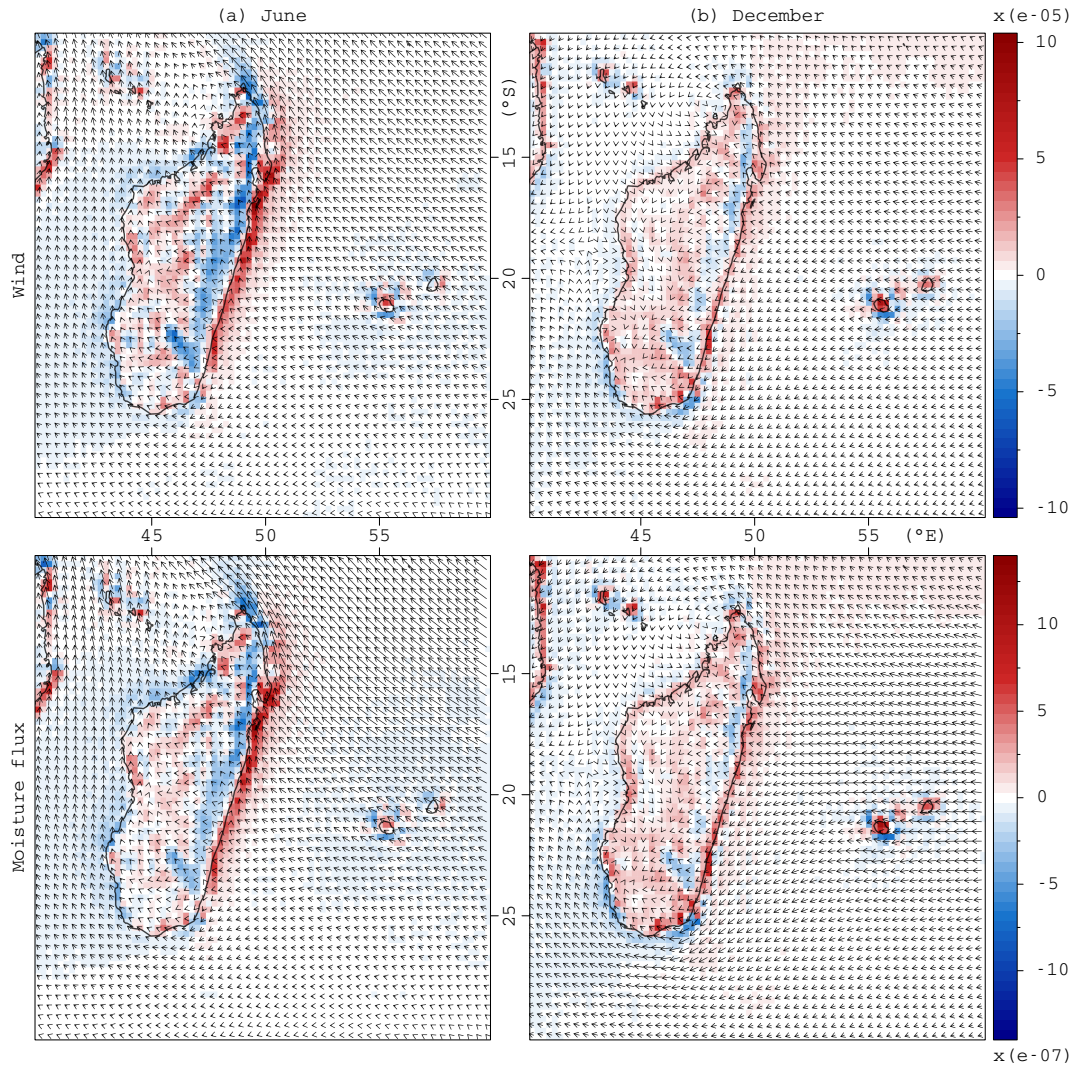


Figure 2: Seasonal characteristics of the wind (\vec{U} , in $\text{m}\cdot\text{s}^{-1}$) and the moisture flux ($q_{sat}\vec{U}$, in $\text{m}\cdot\text{s}^{-1}$), for June (winter) and December (summer). Vectors refers to the eastward and northward components of the two variables (i.e. \vec{U} and $q_{sat}\vec{U}$). Blue-to-red colors are the mass (humidity) flux. Data comes from ERA5 (1979-2018): wind (\vec{U}) is the surface level U and V components of winds at 10 meters; near-surface specific humidity (q_{sat}) is computed from 2 meter dew-point temperature and surface pressure.

93 orography (e.g. André et al., 2019; Mazorra Aguiar et al., 2019; Bessafi et al., 2018a; Wild et al., 2018; Obregón et al.,
 94 2018; Polo et al., 2017; Lauret et al., 2016; Gueymard, 2014; Soubdhan et al., 2009). Their respective influences are
 95 discussed below.

96 2.2. Satellite dataset and pre-processing

97 Satellite Application Facility on Climate Monitoring (CMSAF) produces and provides satellite-derived datasets
 98 of the global energy and water cycle. Several product families of particular interest for the study of SSR are available
 99 such as the Solar surfACE Radiation Heliosat - East (SARAH-E) regional climate data record which is based on

Table 1: Comparison of statistics of Δ_{s-i} ($\text{W}\cdot\text{m}^{-2}$) and $\Delta_{s/i-1}$ (%) for the cases : (1) all hours considered, (2) only 0800 to 1700 RET, (3) all case when *in situ* > 50 $\text{W}\cdot\text{m}^{-2}$ (for hours in 0800-1700 RET) and (4) during TC Bejisa days (from the 1st of January 2014 to the 3rd of January at 1000 RET). *Sd* : standard-deviation; n_h : numbers of hours available all sites combined.

| | All | | 8-17h | | > 50 $\text{W}\cdot\text{m}^{-2}$ | | TC Bejisa | |
|--------|----------------|------------------|----------------|------------------|-----------------------------------|------------------|----------------|------------------|
| | Δ_{s-i} | $\Delta_{s/i-1}$ | Δ_{s-i} | $\Delta_{s/i-1}$ | Δ_{s-i} | $\Delta_{s/i-1}$ | Δ_{s-i} | $\Delta_{s/i-1}$ |
| Max | 1,017 | 11,027 | 1,017 | 11,027 | 962 | 1,323 | 504 | 11,027 |
| 99% | 465 | 452 | 480 | 416 | 483 | 311 | 369 | 2,379 |
| 90% | 185 | 131 | 200 | 113 | 201 | 93 | 143 | 452 |
| 75% | 81 | 45 | 90 | 38 | 90 | 32 | 63 | 207 |
| Median | 14 | 4 | 14 | 3 | 11 | 2 | 31 | 59 |
| 25% | -43 | -11 | -52 | -11 | -55 | -11 | 5 | 4 |
| 10% | -151 | -32 | -167 | -32 | -171 | -32 | -43 | -20 |
| 1% | -458 | -67 | -475 | -66 | -479 | -66 | -230 | -47 |
| Min | -992 | -96 | -992 | -93 | -992 | -93 | -496 | -81 |
| Mean | 16 | 36 | 16 | 30 | 14 | 21 | 40 | 190 |
| Sd | 155 | 117 | 164 | 102 | 166 | 70 | 95 | 528 |
| n_h | 615,288 | | 539,912 | | 522,208 | | 896 | |

100 geostationary METEOSAT satellites. Data from the IODC (Indian Ocean Dipole Coverage) Service are used to
 101 provide the SARAHE data record that covers the Indian Ocean, India and parts of China (Huld et al., 2016). In this
 102 study, this SARAHE record which spans the time period from 1999 to 2016 has been used. Data are extracted over a
 103 3, 355-pixel grid covering the region (53.975, 57.025°E, 22.525, 19.775°S) at the spatial resolution of 0.05°, *ie.* ~ 5.3
 104 km at this location, and with 89 pixels covering the island (Figure 1).

105 A thorough overview of the basic retrieval principle of the Solar surface Radiation Heliosat (SARAH) climate
 106 data records can be found in Müller et al. (2015) and more details for SARAH (Amillo et al., 2014). Information
 107 on aerosols comes from a monthly climatology derived from the Monitoring Atmospheric Composition and Climate
 108 (MACC) reanalysis (Inness et al., 2013; Benedetti et al., 2009; Morcrette et al., 2009; Müller et al., 2015) over the
 109 period 2003-2010, at the spatial resolution of 120 km. Water vapor data are monthly means from the ERA-Interim
 110 reanalysis at the spatial resolution of 79 km (Dee et al., 2011). A topographical correction to the water vapor to
 111 better account for the effects of topography has been applied in the second version of SARAH (SARAH-2; Pfeifroth
 112 et al., 2018), but not in SARAH-E. The complex topography of La Réunion island should then be smoothed, probably
 113 leading to different SSR values at elevated areas where the path to the surface is overestimated. Yet, the use of
 114 SARAH-E still appears better than SARAH-2, in which the position of the island is too close to the picture limits.

115 The reliability of the SARAH-E against *in-situ* measurements has been assessed over India (Riihelä et al., 2018),
 116 China (Wang et al., 2018) and La Réunion (Bessafi et al., 2018b). Riihelä et al. (2018) evaluated the accuracy of

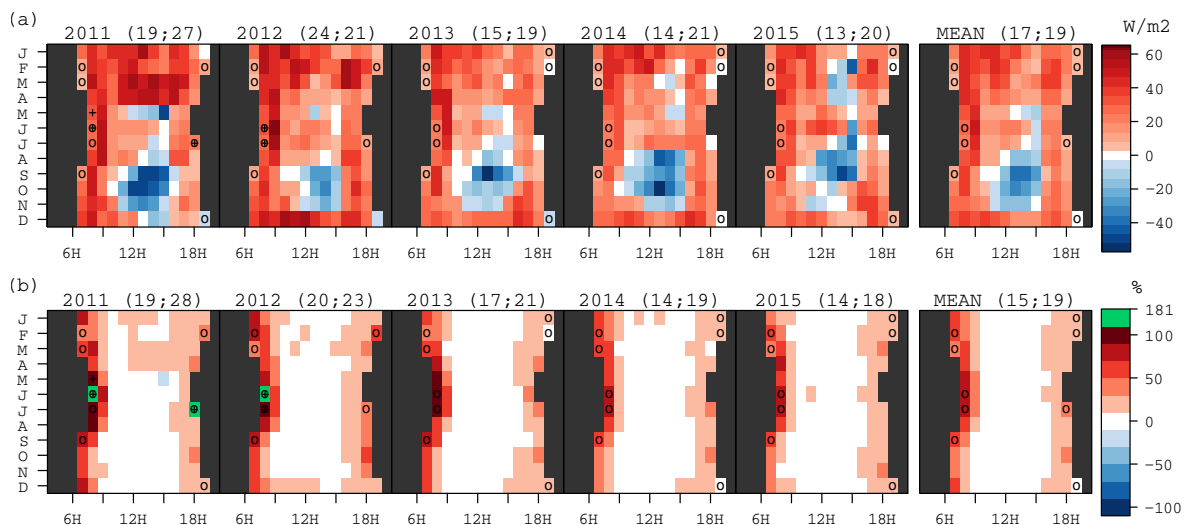


Figure 3: Hourly-monthly means of (a) Δ_{s-i} ($\text{W}\cdot\text{m}^{-2}$) and (b) $\Delta_{s/i-1}$ (%) for each year and for a mean over 2011-2015. The circles \circ locate the *in situ* averages $\leq 50 \text{ W}\cdot\text{m}^{-2}$ and the crosses $+$ locate when $\Delta_{s/i-1} \geq 100\%$. All 32 Météo-France stations are used. Subtitles values in brackets are (mean;standard-deviation).

117 SARAH-E against *in situ* SSR measurements at 17 stations (and 120 station-year) over India (1999-2014) and showed
 118 that, before 2009, SARAH-E estimates are 10-20 % higher than observations. Wang et al. (2018) using 59 stations
 119 for China (1999-2015) also concluded on overestimations (by $7.5 \text{ W}\cdot\text{m}^{-2}$ on average) with the same positive trend in
 120 the differences as that found by Riihelä et al. (2018). Results of these studies are consistent with increasing levels of
 121 Aerosol Optical Depth (AOD) over India and China (Li et al., 2017; Allen et al., 2013). For example, Indian aerosol
 122 daily means are defined with a minima of 0.25 for the AOD at 440 nm and of 0.8 for the AOD at 675 nm during
 123 the years from 2005 to 2016 (Riihelä et al., 2018). In contrast, lower levels of aerosols (mainly biomass and marine
 124 origin) are found over La Réunion (Dufflot et al., 2019; Lamy et al., 2018; Horowitz et al., 2017; Ruiz-Arias et al.,
 125 2016; Gueymard, 2012). Recently, Mallet et al. (2018) compared the aerosol climatology used in SARAH-E to the
 126 AERONET *in situ* measurements over La Réunion (2005-2012) and found well-reproduced variations of the monthly
 127 mean AOD, with a fitting equation slope close to 1. SARAH-E SSR could underestimate La Réunion SSR due to
 128 an overestimated AOD climatology, but aerosol levels there are low (0.148 for MACC, 0.068 for AERONET), with
 129 a quadratic error of 0.084 (Mallet et al., 2018). Hence, SARAH-E should well capture SSR for La Réunion with no
 130 major estimation error due to aerosol levels, even though the size and complexity of the terrain make the evaluation
 131 step there necessary.

132 The accuracy of SARAH-E is assessed over La Réunion through comparisons with in-situ measurements per-
 133 formed by Météo-France. The WMO evaluates each station sensor and site by a classification (WMO, 2014). Site
 134 classification evaluates shades projected by surrounding obstacles while sensor classification evaluates sensor sen-
 135 sitivity measurements. Figure 1 shows the spatial distribution of both classifications for all the SSR Météo-France

136 stations. These are equipped with sensors classified B (ISO 9060:2018) except for two stations with sensors classi-
 137 fied A, and sites are classified from 1 to 3. More characteristics of the Météo-France dataset (instrumentation, sites,
 138 etc.) are given in Bessafi et al. (2018b). Bessafi et al. (2018b) compared monthly means of SARAHE estimates
 139 to Météo-France SSR. This first comparison showed a relative difference of 10 % between the two datasets with
 140 higher divergence locally. Our study further compares the diurnal scales of SSR variations. The comparison here is
 141 performed over the period 2011-2015 with regard to the data at the same Météo-France stations as in Bessafi et al.
 142 (2018b) but at an hourly timescale. The Météo-France SSR measurements have to be converted into hourly means in
 143 $W.m^{-2}$ because they are hourly cumulative values in $J.cm^{-2}$ integrated on the previous hour, sampled every 6 minutes,
 144 while SARAHE estimates of SSR are instantaneous values. For the comparison with observations, we approximated
 145 hourly averaged data from the satellite by, first, temporal interpolation of the hourly clearness index (i.e., the ratio of
 146 the SSR to the radiation at the top of the atmosphere) to generate a 1-min clearness index time series. In a second step,
 147 this time series is multiplied by the top of the atmosphere radiation to result in a 1-min time series of SSR, which, in a
 148 third step, is used to calculate the hourly-averaged SSR data from SARAHE (see also Trolliet et al., 2018). Hereafter,
 149 satellite will refer to SARAHE hourly means and *in situ* will stand for Météo-France surface measurements. For a
 150 given *in situ* station, differences are given by:

$$\Delta_{s-i} = SSR_s - SSR_i, \quad (1)$$

$$\Delta_{s/i-1} = \Delta_{s-i} / SSR_i, \quad (2)$$

151 where SSR_i : the *in situ* SSR at x longitude, y latitude and z elevation, $SSR_i \neq 0$, and SSR_s : the satellite SSR,
 152 extracted by nearest neighbor and converted into hourly means. Table 1 summarizes Δ_{s-i} and $\Delta_{s/i-1}$ statistics of
 153 available hours for all sites combined. Thereafter, we exclusively use the REunion Time (RET) format for hours,
 154 corresponding to GMT+4 (e.g. 0000 UTC is 0400 RET). The two datasets differ by $16W.m^{-2}$ (30 %) on the average
 155 for hours between 0800 and 1700 RET and by $14 W.m^{-2}$ (21 %) after the removal of hours for which *in situ* values
 156 are less than $50W.m^{-2}$. Percents of difference through 1,323 % to 11,027 % occur for *in situ* measurements under 50
 157 $W.m^{-2}$. The largest relative difference (11,027 %) occurs at 0800 RET on January 3, 2014 with *in situ* value at 2.78
 158 $W.m^{-2}$ and satellite at $343 W.m^{-2}$ at a station lying at an altitude of 595 m (Figure 1: “B class” sensor and class 3 site).
 159 During this day, the island was also affected by TC Bejisa (Pianezze et al., 2018). Moreover, differences during the
 160 three days of TC Bejisa are higher than in stable meteorological conditions (Table 1), at $40 \pm 95 W.m^{-2}$ and 190 ± 528
 161 %. The differences between SARAHE and *in-situ* SSR should be analyzed with care, especially since large percent
 162 differences can also result from shaded measures in the early and late hours and from sensor disturbances possibly
 163 caused by violent meteorological conditions.

164 As the present study uses hourly monthly means, Figure 3 displays for each hour and month the averaged differ-
 165 ences of Δ_{s-i} and $\Delta_{s/i-1}$ for all the *in situ* stations. Δ_{s-i} tends to be positive at all times except in the early afternoon
 166 during the winter-to-summer transition months (SON). At this time, La Réunion is under the influence of biomass

167 burning in Madagascar and eastern Africa (Randriambelo et al., 2000; Queface et al., 2011; Lamy et al., 2018). The
 168 overestimation of aerosols in SARAHE should lead to a different behavior, with a global underestimation persisting
 169 during the whole biomass burning period. Low $\Delta_{s/i-1}$ are found at the same period, at $\pm 10\%$ (Figure 3), consistently
 170 with Bessafi et al. (2018b). The largest $\Delta_{s/i-1}$ differences mostly occur in the early morning, during the first full-hour
 171 of daylight (Figure 3). Early and late hours are the most challenging to estimate by SARAHE, and this is when *in*
 172 *situ* measurements are the most probably shaded, which can lead to strong biases. Overall, selecting hours from 0800
 173 RET to 1700 RET centers analysis on daylight (5 hours before to 5 hours after solar noon) and removes most of the
 174 potentially-biased data. These hours are also defined as the photovoltaic use hours by two scenarios with low and high
 175 renewable energy integration (Drouineau et al., 2015). Hence, this study only retains and interprets the grids between
 176 0800 RET through 1700 RET.

177 We also compared SARAHE to the latest version of SARAH (namely SARAH-2; See in Supplementary Ma-
 178 terials). Differences are, in general, very small and both data sets perform comparably with slight advantages for
 179 SARAH-E.

180 2.3. Hierarchical clustering analysis and Ward's clustering

181 Clustering-based approaches help assessing SSR variability by regrouping a large amount of n elements into a
 182 smaller group number. Among these approaches, agglomerative hierarchical clustering (AHC) is used here to compute
 183 all the clustering cases between 1 and n groups. Each of the n clustering cases iterates to optimize an agglomerative
 184 criterion. Here we choose Ward's criterion (Ward Jr, 1963) which minimizes the within-group variance to produce
 185 groups as coherent as possible.

186 This clustering-based approach was successfully used to group non-Gaussian time series of SSR and other climate
 187 parameters such as rainfall: for instance, Willmott and Vernon (1980) defined 10 solar climates over the United
 188 States from averaged global radiations as well as the stations day-to-day perturbations. This method was also used
 189 on 62 stations defined by their 12 monthly means of clearness index over Africa (Diabaté et al., 2004). Lima et al.
 190 (2016) pointed out four homogeneous zones from data of global solar radiation and air temperature at 2 meters high,
 191 using 110 meteorological stations in the tropical North-eastern region of Brazil. Weather regimes were successfully
 192 extracted from rainfall data for La Réunion and South Africa (Crétat et al., 2012, 2019; Morel et al., 2014).

193 In this work, this clustering approach is used to identify SSR zones from the pixels of the SARAHE grid. Each
 194 pixel is characterized by a description of its two orbital components (OC) defined as following :

$$OC(h, m) = \frac{1}{n_y} \sum_{i_y=1}^{n_y} \frac{1}{n_d} \sum_{i_d=1}^{n_d} SSR(h, m, i_d, i_y) \quad (3)$$

195 with (h, m, y, d) for hour, month, year and day and (n_y, n_d) for number of years and days. Considering hours between
 196 0800 RET to 1700 RET, each pixel OC regroups 120 combined averages, *ie.* 12 months \times 10 hours. A first clustering
 197 on all the 3, 355-pixel grid is used to delimit the shape where the island topography changes the global SSR behavior.

198 SSR zones of solar mean behavior are grouped together considering only the 147 pixels inside this area (Figure 1).
199 Others pixels are grouped together to be representative of the sea mean SSR but are excluded for the clustering of
200 solar zones. To our knowledge, clustering of solar radiation have never been made in this way: using the two orbital
201 components together to determine coherent “solar zones”. These zones (obtained here as statistical classes resulting
202 from the grouping of pixels having a similar behavior) are usually defined differently, for instance through monthly
203 means, daily differences or variation metrics (Philippon et al., 2016, 2019; Zagouras et al., 2014; Diabaté et al., 2004;
204 Badosa et al., 2013; de Lima et al., 2019; Watanabe et al., 2016).

205 2.4. Parameters selected for the characterization of clusters

206 Clusters interpretation is done regarding associated solar and topographical parameters. SSR diurnal cycles are
207 computed on monthly bases. Daily amplitudes are averaged over the monthly maxima of the mean SSR diurnal
208 profile. Seasonal amplitudes are the highest differences between 12 monthly maxima of the mean SSR diurnal profile.
209 Topographical parameters (slope, aspect and distance to the sea) are derived from the 30-meters resolution Digital
210 Elevation Model (DEM) from NASA Jet Propulsion Laboratory (2009). Slope is the highest difference on the 4
211 neighbors of each DEM pixels. Aspect gives the direction of the slope. Distance to the sea is calculated as the
212 minimum Euclidean 3-D distance from each 30-meters pixel the DEM to the coastline.

213 These parameters are selected for their relevance for solar energy. The day amplitude reveals the mean solar poten-
214 tial meanly produced in a day while the season amplitude will design the energy systems such as solar farms. Daily
215 mean SSR changes are important for short-term forecast and storage (such as Li-ion batteries). Monthly variation
216 gives indication for the sizing of a solar farm or for hydrogen storage (fuel cells technologies). Topographical param-
217 eters underlines the terrain characteristics, useful for the energy systems installation. They can be seen as indicators
218 of the easy installation and maintenance considering that the biggest cities of the island are concentrated on the coast.

219 3. Local solar context

220 3.1. Mean SSR

221 Mean SSR from 1999 to 2016 of the SARAHE dataset is displayed in Figure 4(b). It is significantly higher over
222 the sea: the lowest 10 % sea-averaged SSR values are similar to the highest 50 % island-averaged SSR values. Only
223 the sea pixels close to the island are impacted by the topography (Figures 1 and 4(b)). Over the island, mean SSR
224 is lower by ~ 19.5 % on average, mostly due to clouds caused by orographic instability. Yet, SSR over the island is
225 highly variable spatially, due to differential cloud cover, with values ranging from 380 to 550 W.m⁻² (Figure 4(b)).
226 The locations of the extreme SSR are indicated in Figure 4(c). Largest SSR (> 520 W.m⁻²) is mostly found over
227 coastal plains, while lowest SSR (< 420 W.m⁻²) is at higher elevations, on both the lee and windward sides of the
228 island (Figure 4(b); Table 2).

229 At the eastern side of La Réunion, the lowest SSR values are found near the two wettest parts (Z_{NE}^- over the NE mid
230 slopes and Z_V^- at the volcano site) where orographic clouds and associated rain develop on the windward slopes facing

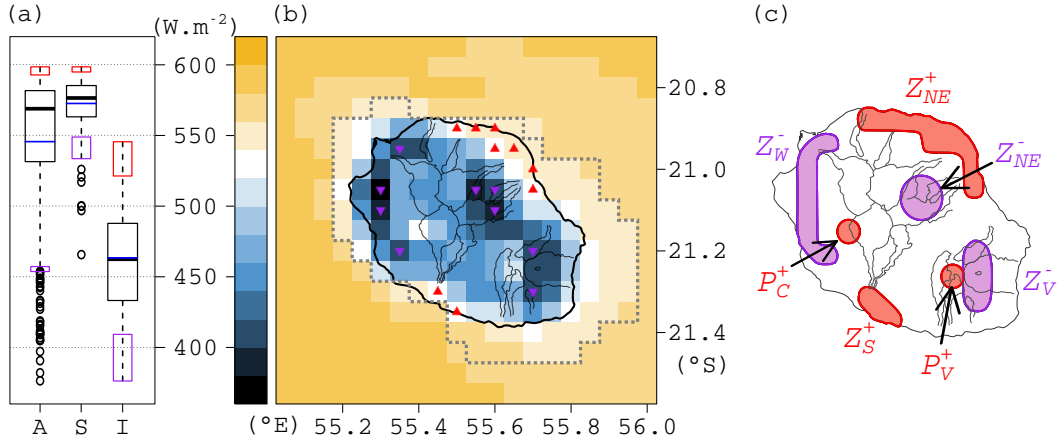


Figure 4: SSR mean characteristics : (a) boxplots for all (A; 360 pixels), sea (S; 271 pixels) and island (I; 89 pixels) fields (*middle black boxes refer to the distribution 50 % around the median in large black lines; blue lines refer to the mean value; the whiskers in black dashed lines indicate the 99 % of the distribution; up (down) rectangles refer to 10 % upper (lower) percentile; circles correspond to outliers, if any*), (b) mean SSR map (*up (down) triangles locate the 10 % highest (lowest) values in red (purple) on the island; the grey dotted line shows the area where the island changes global SSR; the black lines follow island contour (in bold) and ridge lines*) and (c) zones of particular SSR interest (*Z and P for zone and pixel; superscripts + or - denote higher or lower SSR; subscripts indicate location : (N,E,S,W) for cardinal directions and (C,V) for Cilaos, Volcano*).

231 the dominant trade-wind flow (Figure 2; Jumaux et al., 2011). This is also where the main run-of-river hydropower
 232 plants of the island have been installed (Selosse et al., 2018b). At the western side, low SSR is at mid-slopes (~ 499 -m
 233 elevation on average), due to thermally-driven orographic clouds leading to much less rain than further east (Badosa
 234 et al., 2015; Jumaux et al., 2011; Cécé et al., 2016).

235 3.2. Seasonal and diurnal cycles of SSR

236 In this section, we refine analyses at the seasonal and diurnal timescales. The annual mean SSR over the island is
 237 lower in winter ($358 W.m^{-2}$ in June) and larger in summer ($543 W.m^{-2}$ in December: Figure 5(a)). Spatial variability

Table 2: SSR and elevation averaged by zones as defined in Figure 4.

| Zone | SSR ($W.m^{-2}$) | elevation (m) |
|------------|-----------------------|------------------|
| Z_{NE}^+ | 534 | 114 |
| Z_S^+ | 533 | 105 |
| P_C^+ | 520 | 2,100 |
| P_V^+ | 510 | 1,894 |
| Z_W^- | 402 | 499 |
| Z_{NE}^- | 399 | 1,314 |
| Z_V^- | 407 | 1,883 |

238 in SSR is also lower in winter (123 W.m^{-2} in June) and higher in summer (271 W.m^{-2} in November), illustrating that
 239 SSR does not behave similarly throughout the year.

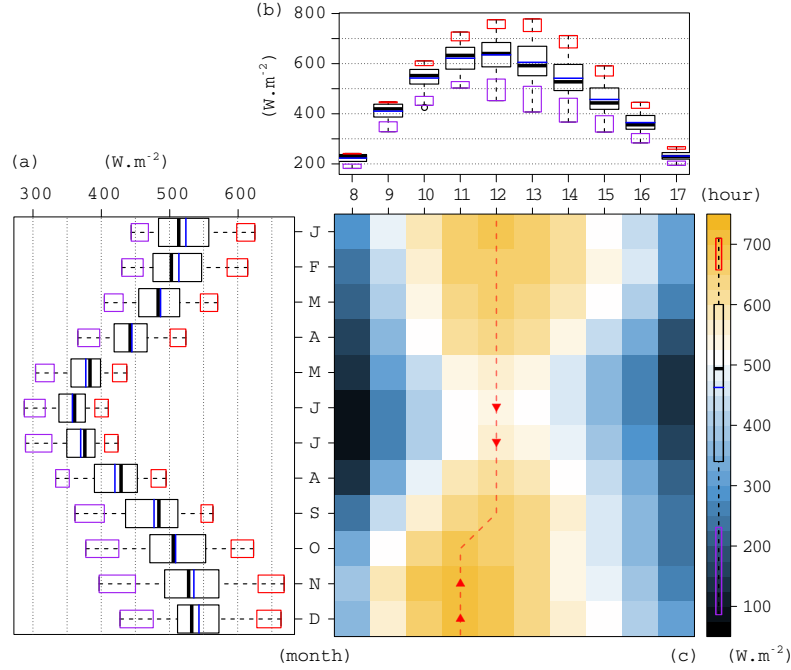


Figure 5: SSR diurnal and seasonal cycles characteristics : In (a) and (b), boxplots detail the SSR mean distribution of the 89 pixels on island (a) for each month and (b) for each hour from 0800 to 1700 RET (*boxplot formalism is the same as in Figure 4*). (c), SSR means (in W.m^{-2}) for each hour-month combination. (*each mean is computed from all the 89 pixels of the island; red dashed lines locate the maximum from all the hours, from 0800 to 1700 RET, for each month; up (down) red triangles locate the two maxima (minima) on the dashed red line*).

240 **Figure 5(b)** summarizes the spatial variability of the annual mean SSR over the island for each hour of the day.
 241 Daily maximum SSR occurs at 1200 RET with a value of 635 W.m^{-2} on average over the island but with a maximum
 242 value of 779 W.m^{-2} at 1300 RET locally. Boxplots for the afternoon hours (1200 to 1500 RET) have a larger spread
 243 (up to 371 W.m^{-2} at 1300 RET) than those for the rest of the day. This denotes larger spatial variability in the middle
 244 of the day than in the early and late hours, consistent with the formation of orographic clouds ([Badosa et al., 2013](#)).

245 **Figure 5(c)** represents the time evolution as a function of both hour and month of the spatial mean SSR for the
 246 island (89 pixels). The shape and timing of the diurnal cycle vary throughout the year. The maximum SSR is generally
 247 at noon, except in late austral winter/early summer (OND) during which it occurs one hour earlier. This is because
 248 clouds develop earlier in the day in summer.

249 **Figure 6** shows the spatial distribution of annual mean hourly SSR. Locations of the minimum and maximum
 250 values as displayed in [Figure 4](#), are likely to vary during the day. On the eastern part of the island, minimum values
 251 of SSR occur in the morning (0800-1100 RET), notably between 0800 and 0900 RET at $Z_{\bar{V}}$ and at 1000 RET at Z_{NE}^-
 252 where SSR remains low during the whole day. On the west, minimum values occur later in the day (1100 RET) over

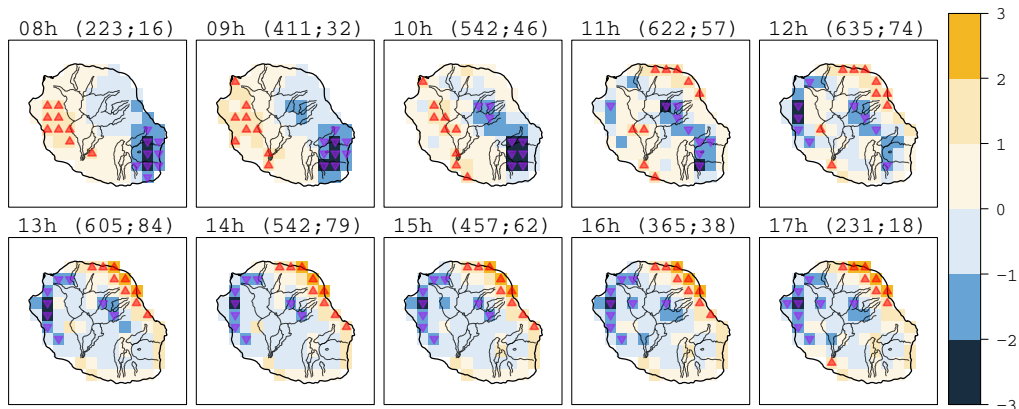


Figure 6: Diurnal evolution of the mean SSR spatial distribution (*unit-less: a spatial standardization is performed over the 89 islands pixels; the black lines show island contour (in bold) and ridge lines; red up (purple down) triangles locate the 10% maxima (minima) of the island; each hour subtitle refers to the island mean and standard deviation (in W.m^{-2}) in bracket; the equivalent non-standardized maps (in W.m^{-2}) are in supplementary materials*).

253 a small area that increases in size during the afternoon, covering pixels at mid slopes and forming thus an elongated
 254 C-shaped pattern following the topography. This east/west differentiation in the diurnal cycle is consistent with the
 255 initiation and evolution of cloud cover (Badosa et al., 2013, 2015; Jumaux et al., 2011). In the early morning, clouds
 256 advected from the sea by the dominant trade winds are often seen along the windward slopes, causing rainfall with
 257 intensities and peak locations depending on the season and the trade-wind inversion height. The leeward side, by
 258 contrast, experiences clear-sky conditions. During the day, orographic clouds with vertical development limited by
 259 the trade-wind inversion layer, form on the mountain slopes due to the combined effects of trade winds and thermal
 260 winds on the windward side and to thermal winds solely on the leeward side. Clouds on that side often spread
 261 towards the coast around or after noon. This spatial extension of clouds is common over islands with a mountainous
 262 topography which involves a return flow created by the combined blocking effect of the orography and the inversion
 263 layer above (Badosa et al., 2015; Cécé et al., 2016; Liu et al., 2015; Garrett, 1980).

264 As the synoptic wind direction changes over the year (Figure 2), so do the windward and the leeward zones, with
 265 major implication on cloud formation (Badosa et al., 2015; Jumaux et al., 2011) and hence on SSR spatial distribution.
 266 Figure 7 shows the particularities of summertime (December) and wintertime (June) diurnal cycles against the annual
 267 mean. It locates the pixels where the SSR means for individual months differ most from the annual mean (Figure 6).
 268 SSR spatial distribution in summer (Figure 7(a)) does not differ significantly from that on the annual mean, except
 269 in the mid-morning when negative values occur at 1000 and 1100 RET in the Z_w^- zone due to earlier development
 270 of local clouds. In contrast in winter (Figure 7(b)), positive values occur in Z_w^- in line with the later development of
 271 orographic clouds. In addition, large negative differences to the annual mean are found in Z_v^- , associated with the
 272 minimum values of SSR throughout the day. This is likely due to orographic rainfall and clouds usually found on

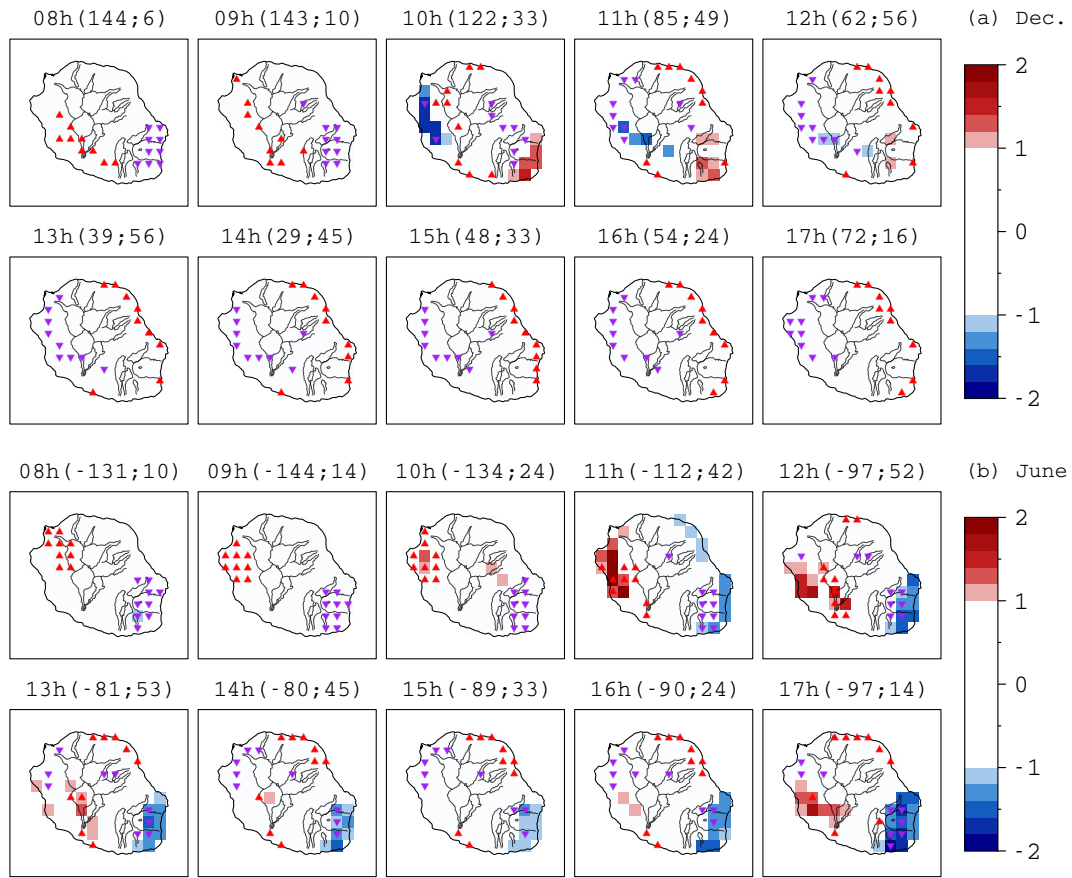


Figure 7: Diurnal standardized SSR maps for (a) December and (b) June after the removal of the annual cycle (in Figure 6). (*unit-less as it is a difference between two standardized maps (annual and month one); the black lines follow island contour (in bold) and ridge lines; red up (purple down) triangles locate the 10% maxima (minima) of the mean SSR of the month; each hour subtitle refers in bracket to the island mean and standard deviation (in $W.m^{-2}$) of the differences between the mean SSR map of the month and the annual mean one; the process to plot the maps combine many steps whom description is done in supplementary materials*).

273 mountainous island slopes, which are fed in moisture by the main trade-wind flow (Chu et al., 2009; Laing, 2004).

274 4. Clustering of solar coherent zones

275 In this section, cluster analysis is used to regionalize spatial features of SSR variability over La Réunion island.
 276 The AHC clustering method is tested for a number of groups ranging from 2 to 18 and on the 147 pixels with similar
 277 monthly mean diurnal cycles of SSR (details in Section 2.3). The number of clusters finally retained is 7 which allows
 278 to structure the solar resource of the island into zones that are fine enough to be linked to the local meteorology but
 279 not too small with a smallest cluster containing 7 pixels. More details of the clustering analysis for different numbers
 280 of groups along with the dendrogram and indices used to choose a cluster number are presented in Supplementary
 281 materials.

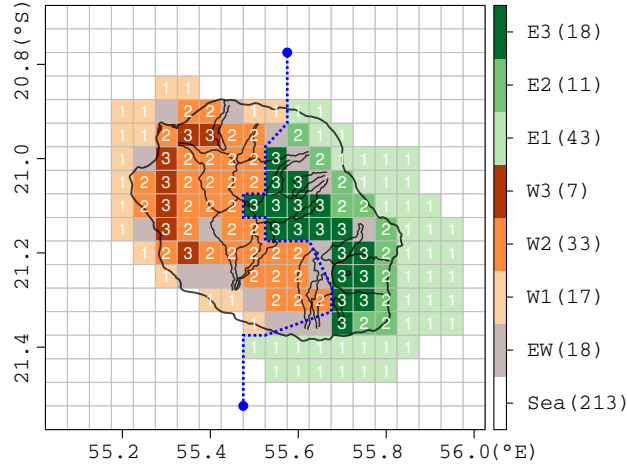


Figure 8: Solar potential micro-climates on La Réunion (each colour refers to one group; for group names, E (green) is for East and W (orange) for West and EW (grey) for East-West; numbers refers from lowest (1) to highest (3) SSR; blue dotted line underlines the east-west clusters limit; numbers in brackets are the number of pixels for each group; Sea group (white) was determined by a first clustering; details in section 2.2).

282 **Figure 8** shows the spatial distribution of the 7 clusters. The pixels are separated graphically to an East and a West
 283 group, (corresponding respectively to clusters E1-3 and W1-3), and located at the eastern (windward) and western
 284 (leeward) sides of the island. The EW cluster can be found over both sides of the island, being mainly coastal on the
 285 leeward side and located at a higher elevation on the opposite side.

286 The eastern (E1-3) clusters are sorted out by increasing elevation and decreasing SSR. As shown in **Table 3**
 287 and **Figure 9**, E1 stretches along the coastline and experiences the highest mean SSR among the eastern clusters,
 288 while E3 is located at higher elevations and displays the lowest SSR on this side of the island. The relationship
 289 between elevation and SSR value is not as straightforward for the western (W1-3) clusters. W3, which experiences
 290 the lowest mean SSR among all clusters and is coincident with Z_W^- zone, lies at lower altitudes than W2 (**Figure 9**).
 291 The Sea and eastern clusters have sensibly larger diurnal than annual cycles of SSR, while western clusters show an
 292 opposite behavior. E1 and Sea clusters have the largest diurnal variations from all clusters and W2 has the largest SSR
 293 seasonality.

We next analyse the diurnal and seasonal cycles of SSR (ie. OC as defined eq. (3)) in each cluster through the difference between the cluster and the island average, and the standard deviation of the cluster. These two metrics are further normalized to the island average as follows:

$$\Delta \overline{OC}(h, m) = \frac{\overline{OC}_{Ci} - \overline{OC}_{island}}{\overline{OC}_{island}}(h, m) \quad (4)$$

and:

$$\sigma(h, m) = \frac{\sigma(OC_{Ci})}{\overline{OC}_{island}}(h, m), \quad (5)$$

294 where (h, m) is for an hour and a month given, \overline{OC}_{Ci} is the OC average over all the pixels of the class i and, \overline{OC}_{island}
 295 over all the 89 pixels of the island (**Figure 5 (c)**) and σ is the standard-deviation operator.

Table 3: Mean parameters group description (topographical parameters : E for elevation (in meters), a for aspect, s for slope (in degrees) and D_{Sea} for sea distance (in kilometers); 3 solar parameters (in $\text{W}\cdot\text{m}^{-2}$) : SSR , A_{Day} day and A_{Season} season amplitudes).

| | SSR | A_{Day} | A_{Season} | D_{Sea} | E | a | s |
|-----|-------|------------------|---------------------|------------------|-------|-----|-----|
| Sea | 581 | 968 | 91 | 1 | 0 | 91 | 0 |
| EW | 490 | 797 | 111 | 6 | 597 | 166 | 12 |
| E1 | 552 | 931 | 100 | 0 | 15 | 96 | 1 |
| E2 | 508 | 864 | 105 | 3 | 272 | 115 | 8 |
| E3 | 419 | 755 | 88 | 12 | 1,289 | 149 | 18 |
| W1 | 542 | 874 | 136 | 1 | 39 | 118 | 2 |
| W2 | 461 | 705 | 160 | 10 | 1,022 | 198 | 19 |
| W3 | 404 | 581 | 120 | 4 | 620 | 222 | 14 |

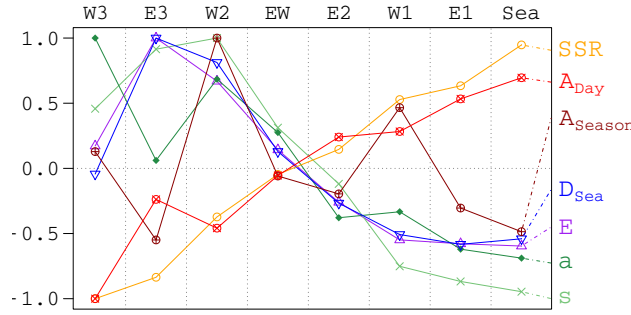


Figure 9: Mean parameters group comparison (sorted by increasing SSR ; each parameter is standardized; the topographical parameters : E for elevation, a for aspect, s for slope and D_{Sea} for sea distance; the 3 solar parameters : SSR , A_{Day} day and A_{Season} season amplitudes).

296 **Figure 10** shows the time evolution of $\Delta\overline{OC}$ and σ for each class. Sea SSR differs most from island SSR in the
 297 afternoon, especially at 1400-1500 RET. This relative difference is larger in summer than in winter, reaching +60 %
 298 ($\sim 330 \text{ W}\cdot\text{m}^{-2}$) in November. The largest $\Delta\overline{OC}$ occurs in November-December for all land clusters, except for W2
 299 and W3 for which it is at its lowest value in October-November. Internal σ is larger in midday and early afternoon in
 300 summer, especially in SON, except for E1 and E2.

301 W3 has a distinctive diurnal cycle of $\Delta\overline{OC}$ which is higher in the morning than the island average, and lower
 302 during the rest of the day. $\Delta\overline{OC}$ reaches a minimum of -34 % ($-185 \text{ W}\cdot\text{m}^{-2}$) at 1400 RET in October. This cluster
 303 is co-located with Z_{W}^- in **Figure 4** where orographic clouds with specific diurnal and seasonal cycles usually develop
 304 (as described in **Figures 6** and **7**). These clouds form earlier in summer (with increased intensity, notably in
 305 October). W2 evolves in a similar way, though the relative differences to the island average are smaller (minimum of
 306 -10 %, $-56 \text{ W}\cdot\text{m}^{-2}$, at 1400 RET in November). Even if orographic clouds occur preferentially at the lower altitudes
 307 of W3, they are likely extended occasionally to W2, particularly in summertime. The seasonality of the $\Delta\overline{OC}$ behavior
 308 of western groups can be related to the Mascarene anticyclone which is further southward and stronger in winter than

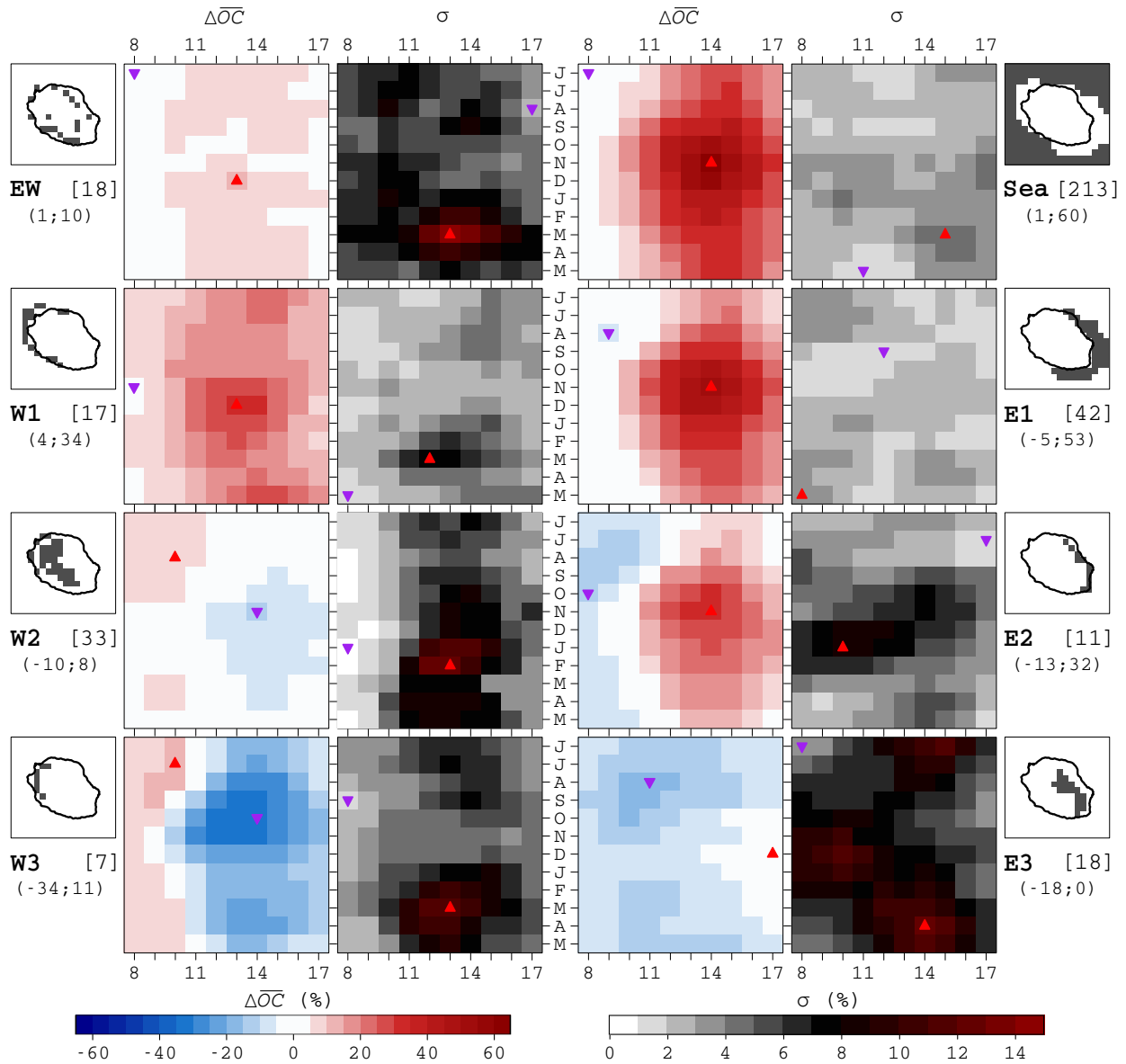


Figure 10: Seasonal and diurnal evolution of each class $\overline{\Delta OC}$ and σ (both percentages are based on the island mean and are expressed in two color-bars (a) for $\overline{\Delta OC}$ and (b) for σ (in Figure 4); up red (down purple) triangles locate the maximum (minimum) by class; for each class, values are (min; max) $\overline{\Delta OC}$ (in %) and [number of pixels])

309 in summer (e.g. Jumaux et al., 2011; Baldy et al., 1996). Cloud processes are then mainly governed by local flows
 310 thanks to higher sea-land differences of temperatures. Higher sea temperatures also provide more humidity to bring at
 311 higher elevations, notably due to the higher elevation of the inversion layer in summer. This induces that orographic
 312 clouds can form more easily and expend over the leeward of the island (Badosa et al., 2015). This process especially
 313 occurs in the afternoon in October-November.

314 Eastern classes have lower $\overline{\Delta OC}$ in the morning than during the rest of the day. For these classes, $\overline{\Delta OC}$ is largest

315 at 1400 RET, except for E3 (maximum at 1700 RET). This cluster displays negative $\overline{\Delta OC}$ at all times, particularly in
316 the mid-morning (1100 RET) where a minimum relative difference of -18% (-103 W.m^{-2}) is found in September.
317 The diurnal evolution of $\overline{\Delta OC}$ for the two western classes, W2 and W3, is the reverse to that of the eastern classes,
318 with positive values in the morning and negative ones during the afternoon. By contrast, western class W1 displays
319 positive $\overline{\Delta OC}$ at all times, with lower values in the early morning and higher values during the afternoon.

320 Solar energy production could greatly benefit from the complementary timing of the mean SSR between the eastern
321 and western sides of the island (Jurasz et al., 2019), reducing its cost through a geographic smoothing (Lave et al.,
322 2012; Perez et al., 2016, 2019). Solar energy systems are mainly installed at locations with high mean SSR (Figure
323 4; OER, 2019). Their mean variations of production can be considered according to the spatial and diurnal-seasonal
324 mean variations described here (Figure 10). They are usually $+30\%$ higher than the mean SSR of the island during
325 summertime afternoon for sites located in Z_{NE}^+ and Z_S^+ (Figure 4; matching with some E1-W1 pixels, see Figure 10).
326 Western production sites, if they can be installed at higher altitudes (W2-W3), could receive $+5\%$ more (-5% less)
327 SSR in the morning (afternoon) than the island mean (Figure 5), with a peak at $+11\%$ (-34%) during summer. The
328 diurnal variation of solar energy could also be stabilized by combining western sites with eastern ones, for instance in
329 zone E2. There, the timing is opposite to the western side, with a mean SSR of -10% ($+25\%$) than the mean SSR of
330 the island during summer morning (afternoon) and a peak of -13% ($+32\%$). Storage of solar production could also
331 smooth these mean variations over seasons and during the day. A systematic overproduction occurring in the morning
332 should then be automatically stored and redelivered during the afternoon, sized according to the mean amplitudes
333 defined. Secondary sources of energy production could be set to deliver the recurrent loss of energy (Kougias et al.,
334 2016; Jurasz and Ciapała, 2018; Jurasz et al., 2019; Jerez et al., 2015). Yet, in addition to these smart grid approaches,
335 temperature and wind velocity should also be considered as they influence the PV production (Mattei et al., 2006;
336 Goossens et al., 2018; Kabeel et al., 2019), paving the way for future research and adjustments to be done over La
337 Réunion and nearby southwest Indian Ocean region.

338 5. Conclusion

339 This work focused on the spatial distribution and timing of the solar resource over the complex topography of the
340 small tropical island of La Réunion in the SWIO. The SARA-E satellite dataset was used here at an hourly timescale
341 over a $0.05^\circ \times 0.05^\circ$ grid of 89 pixels on the island covering the period 1999-2016. It allowed us to delimit the area
342 where the mean solar behavior is influenced by the island topography. The intersection of the seasonal and diurnal
343 scales at particular locations emphasized the necessity to consider jointly the two orbital components to describe the
344 solar behavior. Coherent solar zones were defined by applying an ascending hierarchical clustering on the diurnal
345 and seasonal mean SSR. A side opposition in the SSR patterns in the form of an east-west dipole was found over the
346 island, in accordance with the differentiated windward and leeward cloud processes.

347 This dipole usefully complements the spatial knowledge of the solar potential by their particular timing through

348 months and hours. Solar energy use can be improved considering this side opposition and the complementary timing
349 of both sides of the island. The production and storage sizing should be done with regard to both the seasonal and
350 diurnal amplitudes of SSR. Around these average behaviors, natural and anthropogenic-forced climate variability
351 (from local to global scales, and from synoptic meteorology to climate change) can induce changes to the mean solar
352 resource (Tang et al., 2019). Forecasts can help anticipate drop of solar energy at different horizons (De Felice et al.,
353 2019; Antonanzas et al., 2016). They can prevent the short- and long-term variations which can be compensated
354 by specific storage (e.g. Li-ion batteries, fuel-cells; Akbari et al., 2018). Robustness of smart grids energy systems,
355 under a complex meteorological context such as La Réunion island, has to combine a steady knowledge of the essential
356 cycles of its solar resource, that can strongly vary due to the abrupt topography, to efficient forecasts. The island solar
357 resource can also vary due to large-scale dynamics. Regional-scale atmospheric configurations known to influence
358 local-scale SSR, which first need to be assessed, could then be used to analyze and interpret coarse-resolution global
359 forecasts (e.g. S2S, C3S respectively: Vitart et al., 2017; Manzanas et al., 2019) for PV applications in La Réunion.
360 Analysis of the predictability of these features at various lead-times, from a few hours to a few months in advance,
361 could help adjust energy production or management.

362 **Acknowledgements**

363 The authors acknowledge EUMETSAT for providing the satellite data through the Satellite Application Facility
364 on Climate Monitoring (www.cmsaf.eu) and Météo-France for providing the surface solar irradiance measurements
365 used in this study. Calculations were performed using HPC resources from DNUM CCuB (Centre de Calcul de
366 l'université de Bourgogne). Parts of this work have been done thanks to a PhD fellowship funded by the European
367 Regional Development Fund and Regional Council of La Réunion. Pauline Mialhe gratefully acknowledges Nathalie
368 Philippon, Philippe Blanc, Téléspore Brou and Jordi Badosa for their discussion improving the analyses.

369 **Appendices**

370 Supplementary materials are downloadable on website version of the article at *doi place holder*.

371 **References**

- 372 Akbari, H., Browne, M. C., Ortega, A., Huang, M. J., Hewitt, N. J., Norton, B., McCormack, S. J., May 2018. Efficient energy storage technologies
373 for photovoltaic systems. *Solar Energy*, S0038092X18302846.
- 374 Al Garni, H. Z., Awasthi, A., Nov. 2017. Solar PV power plant site selection using a GIS-AHP based approach with application in Saudi Arabia.
375 *Applied Energy* 206, 1225–1240.
- 376 Allen, R. J., Norris, J. R., Wild, M., Jun. 2013. Evaluation of multidecadal variability in CMIP5 surface solar radiation and inferred underestimation
377 of aerosol direct effects over Europe, China, Japan, and India. *Journal of Geophysical Research: Atmospheres* 118 (12), 6311–6336.

378 Amillo, A., Huld, T., Müller, R., Aug. 2014. A New Database of Global and Direct Solar Radiation Using the Eastern Meteosat Satellite, Models
379 and Validation. *Remote Sensing* 6 (9), 8165–8189.

380 André, M., Perez, R., Soubdhan, T., Schlemmer, J., Calif, R., Monjoly, S., Jan. 2019. Preliminary assessment of two spatio-temporal forecasting
381 technics for hourly satellite-derived irradiance in a complex meteorological context. *Solar Energy* 177, 703–712.

382 Antonanzas, J., Osorio, N., Escobar, R., Urraca, R., Martinez-de-Pison, F., Antonanzas-Torres, F., Oct. 2016. Review of photovoltaic power
383 forecasting. *Solar Energy* 136, 78–111.

384 Badosa, J., Haefelin, M., Chepfer, H., Feb. 2013. Scales of spatial and temporal variation of solar irradiance on Reunion tropical island. *Solar*
385 *Energy* 88, 42–56.

386 Badosa, J., Haefelin, M., Kalecinski, N., Bonnardot, F., Jumaux, G., May 2015. Reliability of day-ahead solar irradiance forecasts on Reunion
387 Island depending on synoptic wind and humidity conditions. *Solar Energy* 115, 306–321.

388 Bağcı, B., Mar. 2009. Towards a Zero Energy Island. *Renewable Energy* 34 (3), 784–789.

389 Baldy, S., Ancellet, G., Bessafi, M., Badr, A., Luk, D. L. S., Oct. 1996. Field observations of the vertical distribution of tropospheric ozone at the
390 island of Reunion (southern tropics). *Journal of Geophysical Research: Atmospheres* 101 (D19), 23835–23849.

391 Bénard-Sora, F., Praene, J. P., Jun. 2016. Territorial analysis of energy consumption of a small remote island: Proposal for classification and
392 highlighting consumption profiles. *Renewable and Sustainable Energy Reviews* 59, 636–648.

393 Bénard-Sora, F., Praene, J. P., Dec. 2018. Sustainable urban planning for a successful energy transition on Reunion Island: From policy intentions
394 to practical achievement. *Utilities Policy* 55, 1–13.

395 Benedetti, A., Morcrette, J.-J., Boucher, O., Dethof, A., Engelen, R. J., Fisher, M., Flentje, H., Huneus, N., Jones, L., Kaiser, J. W., Kinne, S.,
396 Mangold, A., Razinger, M., Simmons, A. J., Suttie, M., Jul. 2009. Aerosol analysis and forecast in the European Centre for Medium-Range
397 Weather Forecasts Integrated Forecast System: 2. Data assimilation. *Journal of Geophysical Research* 114 (D13).

398 Bessafi, M., Oree, V., Hossen Khoodaruth, A. A., Jumaux, G., Bonnardot, F., Jeanty, P., Delsaut, M., Chabriat, J.-P., Zaid Dauhoo, M., Peng, L.,
399 Oct. 2018a. Multifractal Analysis of Daily Global Horizontal Radiation in Complex Topography Island: La Reunion as a Case Study. *Journal*
400 *of Solar Energy Engineering* 141 (3), 031005.

401 Bessafi, M., Oree, V., Khoodaruth, A., Jumaux, G., Bonnardot, F., Jeanty, P., Delsault, M., Chabriat, J.-P., Dauhoo, M., Mar. 2018b. Downscaling
402 solar irradiance using DEM-based model in young volcanic islands with rugged topography. *Renewable Energy*.

403 Bhugwant, C., Cachier, H., Bessafi, M., Leveau, J., Jan. 2000. Impact of traffic on black carbon aerosol concentration at la Reunion Island (Southern
404 Indian Ocean). *Atmospheric Environment* 34 (20), 3463–3473.

405 Blaga, R., Sabadus, A., Stefu, N., Dughir, C., Paulescu, M., Badescu, V., Jan. 2019. A current perspective on the accuracy of incoming solar energy
406 forecasting. *Progress in Energy and Combustion Science* 70, 119–144.

407 Blechinger, P., Cader, C., Bertheau, P., Huyskens, H., Seguin, R., Breyer, C., Nov. 2016. Global analysis of the techno-economic potential of
408 renewable energy hybrid systems on small islands. *Energy Policy* 98, 674–687.

409 Cécé, R., Bernard, D., Brioude, J., Zahibo, N., Aug. 2016. Microscale anthropogenic pollution modelling in a small tropical island during weak
410 trade winds: Lagrangian particle dispersion simulations using real nested LES meteorological fields. *Atmospheric Environment* 139, 98–112.

411 Chu, P.-S., Zhao, X., Ruan, Y., Grubbs, M., Mar. 2009. Extreme Rainfall Events in the Hawaiian Islands. *Journal of Applied Meteorology and*
412 *Climatology* 48 (3), 502–516.

413 Clastres, C., Sep. 2011. Smart grids: Another step towards competition, energy security and climate change objectives. *Energy Policy* 39 (9),
414 5399–5408.

415 Colmenar-Santos, A., Monteagudo-Mencucci, M., Rosales-Asensio, E., de Simón-Martín, M., Pérez-Molina, C., 2019. Optimized design method
416 for storage systems in photovoltaic plants with delivery limitation. *Solar Energy* 180, 468 – 488.

417 Créat, J., Pohl, B., Dieppois, B., Berthou, S., Pergaud, J., Feb. 2019. The Angola Low: Relationship with southern African rainfall and ENSO.
418 *Climate Dynamics* 52 (3-4), 1783–1803.

419 Créat, J., Richard, Y., Pohl, B., Rouault, M., Reason, C., Fauchereau, N., Feb. 2012. Recurrent daily rainfall patterns over South Africa and
420 associated dynamics during the core of the austral summer. *International Journal of Climatology* 32 (2), 261–273.

421 De Felice, M., Soares, M. B., Alessandri, A., Troccoli, A., Nov. 2019. Scoping the potential usefulness of seasonal climate forecasts for solar power
422 management. *Renewable Energy* 142, 215–223.

423 de Lima, F. J. L., Martins, F. R., Costa, R. S., Gonçalves, A. R., dos Santos, A. P. P., Pereira, E. B., Oct. 2019. The seasonal variability and trends
424 for the surface solar irradiation in northeastern region of Brazil. *Sustainable Energy Technologies and Assessments* 35, 335–346.

425 Dee, D. P., Uppala, S. M., Simmons, A. J., Berrisford, P., Poli, P., Kobayashi, S., Andrae, U., Balmaseda, M. A., Balsamo, G., Bauer, P., Bechtold,
426 P., Beljaars, A. C. M., van de Berg, L., Bidlot, J., Bormann, N., Delsol, C., Dragani, R., Fuentes, M., Geer, A. J., Haimberger, L., Healy, S. B.,
427 Hersbach, H., Hólm, E. V., Isaksen, I., Kållberg, P., Köhler, M., Matricardi, M., McNally, A. P., Monge-Sanz, B. M., Morcrette, J.-J., Park,
428 B.-K., Peubey, C., de Rosnay, P., Tavolato, C., Thépaut, J.-N., Vitart, F., Apr. 2011. The ERA-Interim reanalysis: Configuration and performance
429 of the data assimilation system. *Quarterly Journal of the Royal Meteorological Society* 137 (656), 553–597.

430 Diabaté, L., Blanc, P., Wald, L., 2004. Solar radiation climate in Africa. *Solar Energy* 76 (6), 733–744.

431 Diagne, M., David, M., Lauret, P., Boland, J., Schmutz, N., Nov. 2013. Review of solar irradiance forecasting methods and a proposition for
432 small-scale insular grids. *Renewable and Sustainable Energy Reviews* 27, 65–76.

433 Drouineau, M., Assoumou, E., Mazaauric, V., Maïzi, N., Jun. 2015. Increasing shares of intermittent sources in Reunion Island: Impacts on the
434 future reliability of power supply. *Renewable and Sustainable Energy Reviews* 46, 120–128.

435 Dufлот, V., Tulet, P., Flores, O., Barthe, C., Colomb, A., Deguillaume, L., Vařtilingom, M., Perring, A., Huffman, A., Hernandez, M. T., Sellegri,
436 K., Robinson, E., O–Connor, D. J., Gomez, O. M., Burnet, F., Bourriane, T., Strasberg, D., Rocco, M., Bertram, A. K., Chazette, P.,
437 Totems, J., Fournel, J., Stamenoff, P., Metzger, J.-M., Chabasset, M., Rousseau, C., Bourriane, E., Sancelme, M., Delort, A.-M., Wegener, R. E.,
438 Chou, C., Elizondo, P., Aug. 2019. Preliminary results from the FARCE 2015 campaign: Multidisciplinary study of the forest–gas–aerosol–cloud
439 system on the tropical island of La Réunion. *Atmospheric Chemistry and Physics* 19 (16), 10591–10618.

440 Fouilloy, A., Voyant, C., Notton, G., Motte, F., Paoli, C., Nivet, M.-L., Guillot, E., Duchaud, J.-L., Dec. 2018. Solar irradiation prediction with
441 machine learning: Forecasting models selection method depending on weather variability. *Energy* 165, 620–629.

442 Garrett, A. J., Jul. 1980. Orographic Cloud over the Eastern Slopes of Mauna Loa Volcano, Hawaii, Related to Insolation and Wind. *Monthly*
443 *Weather Review* 108 (7), 931–941.

444 Gils, H. C., Simon, S., Feb. 2017. Carbon neutral archipelago – 100% renewable energy supply for the Canary Islands. *Applied Energy* 188,
445 342–355.

446 Goossens, D., Goverde, H., Catthoor, F., Aug. 2018. Effect of wind on temperature patterns, electrical characteristics, and performance of building-
447 integrated and building-applied inclined photovoltaic modules. *Solar Energy* 170, 64–75.

448 Gueymard, C. A., Dec. 2012. Temporal variability in direct and global irradiance at various time scales as affected by aerosols. *Solar Energy*
449 86 (12), 3544–3553.

450 Gueymard, C. A., Mar. 2014. Impact of on-site atmospheric water vapor estimation methods on the accuracy of local solar irradiance predictions.
451 *Solar Energy* 101, 74–82.

452 Guilpart, E., Vimeux, F., Evan, S., Brioude, J., Metzger, J.-M., Barthe, C., Risi, C., Cattani, O., Sep. 2017. The isotopic composition of near-surface
453 water vapor at the Maïdo observatory (Reunion Island, southwestern Indian Ocean) documents the controls of the humidity of the subtropical
454 troposphere: Water Vapor Isotopes in Reunion Island. *Journal of Geophysical Research: Atmospheres* 122 (18), 9628–9650.

455 Hirsch, A., Parag, Y., Guerrero, J., Jul. 2018. Microgrids: A review of technologies, key drivers, and outstanding issues. *Renewable and Sustainable*
456 *Energy Reviews* 90, 402–411.

457 Horowitz, H. M., Garland, R. M., Thatcher, M., Landman, W. A., Dedekind, Z., van der Merwe, J., Engelbrecht, F. A., Nov. 2017. Evaluation of
458 climate model aerosol seasonal and spatial variability over Africa using AERONET. *Atmospheric Chemistry and Physics* 17 (22), 13999–14023.

459 Huld, T., Müller, R., Gracia Amillo, A., Pfeifroth, U., Trentmann, J., 2016. Surface Solar Radiation Data Set - Heliosat, Meteosat-East (SARAH-E)
460 - Edition 1. Satellite Application Facility on Climate Monitoring (CM SAF).

461 Inness, A., Baier, F., Benedetti, A., Bouarar, I., Chabrillat, S., Clark, H., Clerboux, C., Coheur, P., Engelen, R. J., Errera, Q., Flemming, J., George,
462 M., Granier, C., Hadji-Lazarou, J., Huijnen, V., Hurtmans, D., Jones, L., Kaiser, J. W., Kapsomenakis, J., Lefever, K., Leitão, J., Razinger, M.,
463 Richter, A., Schultz, M. G., Simmons, A. J., Suttie, M., Stein, O., Thépaut, J.-N., Thouret, V., Vrekoussis, M., Zerefos, C., the MACC team,

464 Apr. 2013. The MACC reanalysis: An 8 yr data set of atmospheric composition. *Atmospheric Chemistry and Physics* 13 (8), 4073–4109.

465 IPCC-WGII, 2014. IPCC, 2014: Summary for policymakers. *Climate change*.

466 Jerez, S., Tobin, I., Vautard, R., Montávez, J. P., López-Romero, J. M., Thais, F., Bartok, B., Christensen, O. B., Colette, A., Déqué, M., Nikulin,
467 G., Kotlarski, S., van Meijgaard, E., Teichmann, C., Wild, M., Dec. 2015. The impact of climate change on photovoltaic power generation in
468 Europe. *Nature Communications* 6, 10014.

469 Jumaux, G., Quetelard, H., Roy, D., 2011. Atlas climatique de la Réunion. Météo-France, Direction interrégionale de la Réunion, Sainte-Clotilde
470 (Réunion).

471 Jurasz, J., Canales, F., Kies, A., Guezgouz, M., Beluco, A., 2019. A review on the complementarity of renewable energy sources: Concept, metrics,
472 application and future research directions. arXiv preprint arXiv:1904.01667.

473 Jurasz, J., Ciapała, B., Oct. 2018. Solar–hydro hybrid power station as a way to smooth power output and increase water retention. *Solar Energy*
474 173, 675–690.

475 Kabeel, A., Abdelgaied, M., Sathyamurthy, R., 2019. A comprehensive investigation of the optimization cooling technique for improving the
476 performance of PV module with reflectors under Egyptian conditions. *Solar Energy* 186, 257–263.

477 Koo, C., Li, W., Cha, S. H., Zhang, S., Apr. 2019. A novel estimation approach for the solar radiation potential with its complex spatial pattern via
478 machine-learning techniques. *Renewable Energy* 133, 575–592.

479 Kougiás, I., Szabó, S., Monforti-Ferrario, F., Huld, T., Bódis, K., 2016. A methodology for optimization of the complementarity between small-
480 hydropower plants and solar PV systems. *Renewable Energy* 87, 1023 – 1030, optimization Methods in Renewable Energy Systems Design.

481 Krajačić, G., Duić, N., Carvalho, M. d. G., Feb. 2011. How to achieve a 100% RES electricity supply for Portugal? *Applied Energy* 88 (2),
482 508–517.

483 Kuang, Y., Zhang, Y., Zhou, B., Li, C., Cao, Y., Li, L., Zeng, L., Jun. 2016. A review of renewable energy utilization in islands. *Renewable and*
484 *Sustainable Energy Reviews* 59, 504–513.

485 Laing, A. G., Aug. 2004. Cases of Heavy Precipitation and Flash Floods in the Caribbean during El Niño Winters. *Journal of Hydrometeorology*
486 5 (4), 577–594.

487 Lamy, K., Portafaix, T., Brogniez, C., Godin-Beekmann, S., Bencherif, H., Morel, B., Pazmino, A., Metzger, J. M., Auriol, F., Deroo, C., Duflot, V.,
488 Goloub, P., Long, C. N., Jan. 2018. Ultraviolet radiation modelling from ground-based and satellite measurements on Reunion Island, southern
489 tropics. *Atmospheric Chemistry and Physics* 18 (1), 227–246.

490 Lauret, P., Perez, R., Mazorra Aguiar, L., Tapachès, E., Diagne, H. M., David, M., Feb. 2016. Characterization of the intraday variability regime of
491 solar irradiation of climatically distinct locations. *Solar Energy* 125, 99–110.

492 Lave, M., Kleissl, J., Arias-Castro, E., Aug. 2012. High-frequency irradiance fluctuations and geographic smoothing. *Solar Energy* 86 (8), 2190–
493 2199.

494 Leroux, M.-D., Meister, J., Mekies, D., Dorla, A.-L., Caroff, P., Apr. 2018. A Climatology of Southwest Indian Ocean Tropical Systems: Their
495 Number, Tracks, Impacts, Sizes, Empirical Maximum Potential Intensity, and Intensity Changes. *Journal of Applied Meteorology and Clima-*
496 *tology* 57 (4), 1021–1041.

497 Lesouëf, D., Gheusi, F., Delmas, R., Escobar, J., Jan. 2011. Numerical simulations of local circulations and pollution transport over Reunion Island.
498 *Annales Geophysicae* 29 (1), 53–69.

499 Li, C., McLinden, C., Fioletov, V., Krotkov, N., Carn, S., Joiner, J., Streets, D., He, H., Ren, X., Li, Z., Dickerson, R. R., Dec. 2017. India Is
500 Overtaking China as the World’s Largest Emitter of Anthropogenic Sulfur Dioxide. *Scientific Reports* 7 (1).

501 Lima, F. J., Martins, F. R., Pereira, E. B., Lorenz, E., Heinemann, D., Mar. 2016. Forecast for surface solar irradiance at the Brazilian Northeastern
502 region using NWP model and artificial neural networks. *Renewable Energy* 87, 807–818.

503 Liu, J.-W., Xie, S.-P., Zhang, S.-P., Jan. 2015. Effects of the Hawaiian Islands on the vertical structure of low-level clouds from CALIPSO lidar:
504 Hawaiian Clouds. *Journal of Geophysical Research: Atmospheres* 120 (1), 215–228.

505 Mallet, P.-É., Pujol, O., Brioude, J., Evan, S., Jensen, A., Jun. 2018. Marine aerosol distribution and variability over the pristine Southern Indian
506 Ocean. *Atmospheric Environment* 182, 17–30.

507 Manzanas, R., Gutiérrez, J. M., Bhend, J., Hemri, S., Doblas-Reyes, F. J., Torralba, V., Penabad, E., Brookshaw, A., Aug. 2019. Bias adjustment and
508 ensemble recalibration methods for seasonal forecasting: A comprehensive intercomparison using the C3S dataset. *Climate Dynamics* 53 (3-4),
509 1287–1305.

510 Marquez, R., Coimbra, C. F. M., Oct. 2012. Proposed Metric for Evaluation of Solar Forecasting Models. *Journal of Solar Energy Engineering*
511 135 (1), 011016.

512 Mattei, M., Notton, G., Cristofari, C., Muselli, M., Poggi, P., Apr. 2006. Calculation of the polycrystalline PV module temperature using a simple
513 method of energy balance. *Renewable Energy* 31 (4), 553–567.

514 Mazorra Aguiar, L., Polo, J., Vindel, J., Oliver, A., May 2019. Analysis of satellite derived solar irradiance in islands with site adaptation techniques
515 for improving the uncertainty. *Renewable Energy* 135, 98–107.

516 Mejia, J. F., Giordano, M., Wilcox, E., Mar. 2018. Conditional summertime day-ahead solar irradiance forecast. *Solar Energy* 163, 610–622.

517 Mendoza-Vizcaino, J., Raza, M., Sumper, A., Dfáz-González, F., Galceran-Arellano, S., Jan. 2019. Integral approach to energy planning and
518 electric grid assessment in a renewable energy technology integration for a 50/50 target applied to a small island. *Applied Energy* 233-234,
519 524–543.

520 Merceron, S., Nov. 2017. La population réunionnaise à l’horizon 2050. Autant de seniors que de jeunes. *Analyses La Réunion* 29, INSEE.

521 Meschede, H., Child, M., Breyer, C., Jun. 2018. Assessment of sustainable energy system configuration for a small Canary island in 2030. *Energy*
522 *Conversion and Management* 165, 363–372.

523 Meschede, H., Holzapfel, P., Kadelbach, F., Hesselbach, J., Aug. 2016. Classification of global island regarding the opportunity of using RES.
524 *Applied Energy* 175, 251–258.

525 Morcrette, J.-J., Boucher, O., Jones, L., Salmond, D., Bechtold, P., Beljaars, A., Benedetti, A., Bonet, A., Kaiser, J. W., Razinger, M., Schulz, M.,
526 Serrar, S., Simmons, A. J., Sofiev, M., Suttie, M., Tompkins, A. M., Untch, A., Mar. 2009. Aerosol analysis and forecast in the European Centre
527 for Medium-Range Weather Forecasts Integrated Forecast System: Forward modeling. *Journal of Geophysical Research* 114 (D6).

528 Morel, B., Pohl, B., Richard, Y., Bois, B., Bessafi, M., Aug. 2014. Regionalizing Rainfall at Very High Resolution over La Réunion Island Using a
529 Regional Climate Model. *Monthly Weather Review* 142 (8), 2665–2686.

530 Müller, R., Pfeifroth, U., Träger-Chatterjee, C., Trentmann, J., Cremer, R., Jun. 2015. Digging the METEOSAT Treasure—3 Decades of Solar
531 Surface Radiation. *Remote Sensing* 7 (6), 8067–8101.

532 NASA Jet Propulsion Laboratory, 2009. ASTER Global Digital Elevation Model. NASA JPL.

533 Notton, G., Jul. 2015. Importance of islands in renewable energy production and storage: The situation of the French islands. *Renewable and*
534 *Sustainable Energy Reviews* 47, 260–269.

535 Obara, S., Sato, K., Utsugi, Y., Oct. 2018. Study on the operation optimization of an isolated island microgrid with renewable energy layout
536 planning. *Energy* 161, 1211–1225.

537 Obregón, M., Costa, M., Silva, A., Serrano, A., Nov. 2018. Impact of aerosol and water vapour on SW radiation at the surface: Sensitivity study
538 and applications. *Atmospheric Research* 213, 252–263.

539 OER, 2018. Bilan énergétique de La Réunion 2017 - Édition 2018. Tech. rep.

540 Olowu, T. O., Sundararajan, A., Moghaddami, M., Sarwat, A. I., 2018. Future challenges and mitigation methods for high photovoltaic penetration:
541 A survey. *Energies* 11 (7), 1782.

542 Perdigão, J., Salgado, R., Magarreiro, C., Soares, P. M., Costa, M. J., Dasari, H. P., Dec. 2017. An Iberian climatology of solar radiation obtained
543 from WRF regional climate simulations for 1950–2010 period. *Atmospheric Research* 198, 151–162.

544 Perez, M., Perez, R., Rábago, K. R., Putnam, M., Mar. 2019. Overbuilding & curtailment: The cost-effective enablers of firm PV generation. *Solar*
545 *Energy* 180, 412–422.

546 Perez, M. J., Fthenakis, V. M., 2015. On the spatial decorrelation of stochastic solar resource variability at long timescales. *Solar Energy* 117, 46 –
547 58.

548 Perez, R., Rábago, K. R., Trahan, M., Rawlings, L., Norris, B., Hoff, T., Putnam, M., Perez, M., Sep. 2016. Achieving very high PV penetration –
549 The need for an effective electricity remuneration framework and a central role for grid operators. *Energy Policy* 96, 27–35.

550 Pfeifroth, U., Sanchez-Lorenzo, A., Manara, V., Trentmann, J., Hollmann, R., Feb. 2018. Trends and Variability of Surface Solar Radiation in
551 Europe Based On Surface- and Satellite-Based Data Records: TRENDS AND VARIABILITY OF SURFACE SOLAR RADIATION. *Journal*
552 *of Geophysical Research: Atmospheres*.

553 Philippon, N., Cornu, G., Monteil, L., Gond, V., Moron, V., Pergaud, J., Sèze, G., Bigot, S., Camberlin, P., Doumenge, C., Fayolle, A., Ngomanda,
554 A., Mar. 2019. The light-deficient climates of western Central African evergreen forests. *Environmental Research Letters* 14 (3), 034007.

555 Philippon, N., de Lapparent, B., Gond, V., Sèze, G., Martiny, N., Camberlin, P., Cornu, G., Morel, B., Moron, V., Bigot, S., Brou, T., Dubreuil, V.,
556 Jun. 2016. Analysis of the diurnal cycles for a better understanding of the mean annual cycle of forests greenness in Central Africa. *Agricultural*
557 *and Forest Meteorology* 223, 81–94.

558 Pianezze, J., Barthe, C., Bielli, S., Tulet, P., Jullien, S., Cambon, G., Bousquet, O., Claeys, M., Cordier, E., Mar. 2018. A New Coupled Ocean-
559 Waves-Atmosphere Model Designed for Tropical Storm Studies: Example of Tropical Cyclone Bejisa (2013-2014) in the South-West Indian
560 Ocean. *Journal of Advances in Modeling Earth Systems* 10 (3), 801–825.

561 Pohl, B., Morel, B., Barthe, C., Bousquet, O., Nov. 2016. Regionalizing Rainfall at Very High Resolution over La Réunion Island: A Case Study
562 for Tropical Cyclone Ando. *Monthly Weather Review* 144 (11), 4081–4099.

563 Polo, J., Ballestrín, J., Alonso-Montesinos, J., López-Rodríguez, G., Barbero, J., Carra, E., Fernández-Reche, J., Bosch, J. L., Battles, F. J., Nov.
564 2017. Analysis of solar tower plant performance influenced by atmospheric attenuation at different temporal resolutions related to aerosol optical
565 depth. *Solar Energy* 157, 803–810.

566 Polo, J., Bernardos, A., Navarro, A., Fernandez-Peruchena, C., Ramírez, L., Guisado, M. V., Martínez, S., Jul. 2015. Solar resources and power
567 potential mapping in Vietnam using satellite-derived and GIS-based information. *Energy Conversion and Management* 98, 348–358.

568 Praene, J. P., David, M., Sinama, F., Morau, D., Marc, O., Jan. 2012. Renewable energy: Progressing towards a net zero energy island, the case of
569 Reunion Island. *Renewable and Sustainable Energy Reviews* 16 (1), 426–442.

570 Právělie, R., Patriche, C., Bandoc, G., Feb. 2019. Spatial assessment of solar energy potential at global scale. A geographical approach. *Journal of*
571 *Cleaner Production* 209, 692–721.

572 Queface, A. J., Piketh, S. J., Eck, T. F., Tsay, S.-C., Mavume, A. F., Jun. 2011. Climatology of aerosol optical properties in Southern Africa.
573 *Atmospheric Environment* 45 (17), 2910–2921.

574 Quetelard, H., Bessemoulin, P., Cerveny, R. S., Peterson, T. C., Burton, A., Boodhoo, Y., May 2009. Extreme Weather: World-Record Rainfalls
575 During Tropical Cyclone Gamede. *Bulletin of the American Meteorological Society* 90 (5), 603–608.

576 Raghoo, P., Surroop, D., Wolf, F., Leal Filho, W., Jeetah, P., Delakowitz, B., Aug. 2018. Dimensions of energy security in Small Island Developing
577 States. *Utilities Policy* 53, 94–101.

578 Randriambelo, T., Baray, J.-L., Baldy, S., May 2000. Effect of biomass burning, convective venting, and transport on tropospheric ozone over the
579 Indian Ocean: Reunion Island field observations. *Journal of Geophysical Research: Atmospheres* 105 (D9), 11813–11832.

580 Réchou, A., Flores, O., Jumaux, G., Duflot, V., Bousquet, O., Pouppeville, C., Bonnardot, F., Apr. 2019. Spatio-temporal variability of rainfall
581 in a high tropical island: Patterns and large-scale drivers in Réunion Island. *Quarterly Journal of the Royal Meteorological Society* 145 (720),
582 893–909.

583 RégionRéunion, 2003a. Agenda 21 - île de La Réunion. Tech. rep., Région Réunion.

584 RégionRéunion, 2003b. Agenda 21 - île de La Réunion - Présentation des fiches actions 2002-2003. Tech. rep.

585 Riihelä, A., Kallio, V., Devraj, S., Sharma, A., Lindfors, A. V., 2018. Validation of the SARAH-E Satellite-Based Surface Solar Radiation Estimates
586 over India. *Remote Sensing* 10 (3), 392.

587 Ruiz-Arias, J. A., Gueymard, C. A., Santos-Alamillos, F. J., Pozo-Vázquez, D., Sep. 2016. Worldwide impact of aerosol's time scale on the
588 predicted long-term concentrating solar power potential. *Scientific Reports* 6 (1).

589 Scolah, H., Sopinka, A., van Kooten, G. C., Mar. 2012. The economics of storage, transmission and drought: Integrating variable wind power into
590 spatially separated electricity grids. *Energy Economics* 34 (2), 536–541.

591 Selosse, S., Garabedian, S., Ricci, O., Maïzi, N., Jun. 2018a. The renewable energy revolution of reunion island. *Renewable and Sustainable Energy*
592 *Reviews* 89, 99–105.

593 Selosse, S., Ricci, O., Garabedian, S., Maïzi, N., Dec. 2018b. Exploring sustainable energy future in Reunion Island. *Utilities Policy* 55, 158–166.

594 Sen, S., Ganguly, S., Das, A., Sen, J., Dey, S., Oct. 2016. Renewable energy scenario in India: Opportunities and challenges. *Journal of African*
595 *Earth Sciences* 122, 25–31.

596 Singh, R., Jan. 2018. Energy sufficiency aspirations of India and the role of renewable resources: Scenarios for future. *Renewable and Sustainable*
597 *Energy Reviews* 81, 2783–2795.

598 Singh Doorga, J. R., Rughooputh, S. D., Boojhawon, R., Feb. 2019. High resolution spatio-temporal modelling of solar photovoltaic potential for
599 tropical islands: Case of Mauritius. *Energy* 169, 972–987.

600 Sisavath, E., Babonneau, N., Saint-Ange, F., Bachèlery, P., Jorry, S. J., Deplus, C., De Voogd, B., Savoye, B., Oct. 2011. Morphology and
601 sedimentary architecture of a modern volcanoclastic turbidite system: The Cilaos fan, offshore La Réunion Island. *Marine Geology* 288 (1-4),
602 1–17.

603 Soler, O., 1997. Atlas Climatique de La Réunion. Météo-France, Direction interrégionale de la Réunion.

604 Soubdhan, T., Emilion, R., Calif, R., Jul. 2009. Classification of daily solar radiation distributions using a mixture of Dirichlet distributions. *Solar*
605 *Energy* 83 (7), 1056–1063.

606 Surroop, D., Raghoo, P., Wolf, F., Shah, K. U., Jeetah, P., Sep. 2018. Energy access in Small Island Developing States: Status, barriers and policy
607 measures. *Environmental Development* 27, 58–69.

608 Tang, C., Morel, B., Wild, M., Pohl, B., Abiodun, B., Lennard, C., Bessafi, M., Aug. 2019. Numerical simulation of surface solar radiation over
609 Southern Africa. Part 2: Projections of regional and global climate models. *Climate Dynamics* 53 (3-4), 2197–2227.

610 Timilsina, G. R., Shah, K. U., Nov. 2016. Filling the gaps: Policy supports and interventions for scaling up renewable energy development in Small
611 Island Developing States. *Energy Policy* 98, 653–662.

612 Trolliet, M., Walawender, J. P., Bourlès, B., Boilley, A., Trentmann, J., Blanc, P., Lefèvre, M., Wald, L., Sep. 2018. Downwelling surface solar
613 irradiance in the tropical Atlantic Ocean: A comparison of re-analyses and satellite-derived data sets to PIRATA measurements. *Ocean Science*
614 14 (5), 1021–1056.

615 Unamuno, E., Barrena, J. A., Dec. 2015. Hybrid ac/dc microgrids—Part I: Review and classification of topologies. *Renewable and Sustainable*
616 *Energy Reviews* 52, 1251–1259.

617 Urquhart, B., Sengupta, M., Keller, J., Sep. 2013. Optimizing geographic allotment of photovoltaic capacity in a distributed generation setting:
618 Optimizing geographic allotment of PV capacity. *Progress in Photovoltaics: Research and Applications* 21 (6), 1276–1285.

619 Vèrèmes, H., Listowski, C., Delanoë, J., Barthe, C., Tulet, P., Bonnardot, F., Roy, D., Aug. 2019. Spatial and seasonal variability of clouds over the
620 South-West Indian Ocean based on the DARDAR mask product. *Quarterly Journal of the Royal Meteorological Society*, qj.3640.

621 Vitart, F., Ardilouze, C., Bonet, A., Brookshaw, A., Chen, M., Codorean, C., Déqué, M., Ferranti, L., Fucile, E., Fuentes, M., Hendon, H., Hodgson,
622 J., Kang, H.-S., Kumar, A., Lin, H., Liu, G., Liu, X., Malguzzi, P., Mallas, I., Manoussakis, M., Mastrangelo, D., MacLachlan, C., McLean,
623 P., Minami, A., Mladek, R., Nakazawa, T., Najm, S., Nie, Y., Rixen, M., Robertson, A. W., Ruti, P., Sun, C., Takaya, Y., Tolstykh, M., Venuti,
624 F., Waliser, D., Woolnough, S., Wu, T., Won, D.-J., Xiao, H., Zaripov, R., Zhang, L., Jan. 2017. The Subseasonal to Seasonal (S2S) Prediction
625 Project Database. *Bulletin of the American Meteorological Society* 98 (1), 163–173.

626 Wang, Y., Trentmann, J., Yuan, W., Wild, M., Dec. 2018. Validation of CM SAF CLARA-A2 and SARA-E Surface Solar Radiation Datasets over
627 China. *Remote Sensing* 10 (12), 1977.

628 Ward Jr, J. H., 1963. Hierarchical grouping to optimize an objective function. *Journal of the American statistical association* 58 (301), 236–244.

629 Watanabe, T., Takamatsu, T., Nakajima, T. Y., Oct. 2016. Evaluation of Variation in Surface Solar Irradiance and Clustering of Observation Stations
630 in Japan. *Journal of Applied Meteorology and Climatology* 55 (10), 2165–2180.

631 Wegertseder, P., Lund, P., Mikkola, J., García Alvarado, R., Oct. 2016. Combining solar resource mapping and energy system integration methods
632 for realistic valuation of urban solar energy potential. *Solar Energy* 135, 325–336.

633 Weisser, D., Jan. 2004. On the economics of electricity consumption in small island developing states: A role for renewable energy technologies?
634 *Energy Policy* 32 (1), 127–140.

635 Wild, M., Hakuba, M. Z., Folini, D., Dörig-Ott, P., Schär, C., Kato, S., Long, C. N., Aug. 2018. The cloud-free global energy balance and inferred

636 cloud radiative effects: An assessment based on direct observations and climate models. *Climate Dynamics*.

637 Willmott, C. J., Vernon, M. T., 1980. Solar climates of the conterminous united states: A preliminary investigation. *Solar Energy* 24 (3), 295–303.

638 WMO, 2014. *Guide to Meteorological Instruments and Methods of Observation* WMO-No. 8.

639 Zagouras, A., Pedro, H. T., Coimbra, C. F., Dec. 2014. Clustering the solar resource for grid management in island mode. *Solar Energy* 110,

640 507–518.

Coherent zones of mean Solar Surface Radiation (SSR) on a tropical island

the case of La Réunion

SSR West Zones
on the leeward side

SSR East Zones
on the windward side

